Master's thesis

NTNU
Norwegian University of Science and Technology
Faculty of Natural Sciences
Department of Physics

Simen Johnsrud

Molecular Beam Epitaxy Growth of the Kagome magnet system Fe-Sn

Master's thesis in Applied Physics and Mathematics
Supervisor: Christoph Brüne
June 2022

NTNU
Norwegian University of
Science and Technology

Simen Johnsrud

Molecular Beam Epitaxy Growth of the Kagome magnet system Fe-Sn

Master’s thesis in Applied Physics and Mathematics
Supervisor: Christoph Brüne
June 2022

Norwegian University of Science and Technology
Faculty of Natural Sciences
Department of Physics

NTNU
Norwegian University of
Science and Technology

Contents

Acknowledgements

I would like to thank the MBE Group from the Center for Quantum Spintronics, Department of Physics, Norwegian University of Science and Technology (NTNU). Especially Christoph Brüne, my supervisor. Payel Chatterjee for specific guidance in Fe-Sn research, and for providing general guidance in Molecular beam epitaxy research, together with Matthias Hartl and Longfei He. And also specifically Payel Chatterjee for providing SEM measurements, and Stefanie S. Brinkman and Matthias Hartl for providing XRD measurements.

Abstract

The Kagome magnet system Fe-Sn is a set of crystal structures consisting of stacked layers of Fe_3Sn and Sn_2. Magnets in this system have been found to exhibit exotic quantum properties, which may have applications in novel spintronic components. The most studied phase of this system is Fe_3Sn_2, which has been proven to host magnetic skyrmions at room temperature. Magnetic skyrmions are topological structures in the magnetization field of a condensed matter system that can be created, moved and deleted using electric or magnetic fields. This makes them a potential candidate for encoding data, both for storage and for transfer, for example in racetrack memory systems [1].

This work attempts to grow Fe-Sn thin film crystals using molecular beam epitaxy. Si(111) and GaAs(111) substrates were used to grow the films. The Si(111) substrate was shown to react with the iron, causing the formation of $FeSi_2$ and β-tin, which suppressed Fe_3Sn_2 growth. The GaAs(111) substrates resulted in the growth of Fe_3Sn_2, evidenced by the occurrence of (009) Fe_3Sn_2 peak in the XRD measurements. However, with the presence of other unidentified phases. The films showed varying degrees of surface roughness, but no set of parameters achieved an atomically flat 2D surface.

Chapter 1

Introduction

The digital revolution is the period of rapid innovation, mainly in the fields electronics and material science, that has been going on since the middle of the 20th century. The main driver of this revolution has been to continuously scale down the size and the power requirements of the components used in digital electronics, especially the metal-oxide-semiconductor field-effect transistor (MOSFET), which is central in integrated circuits (IC). The down-scaling in size of MOSFET components in integrated circuits were observed to be exponential, and Gordon Moore, co-founder of Fairchild Semiconductor and Intel, predicted in 1965 that the number of transistors on a dense IC doubles every two years [2]. This prediction has since been coined *Moore's law*, and still holds true today. The accompanying observation regarding the down-scaling of power requirement of transistors is called *Dennard scaling*, and is based on a paper from 1974 by Robert H. Dennard et al. [3]. This law held true for several decades, however, around 2006, it broke down. The main reason for the breakdown on the small scales is believed to be current leakage due to quantum effects [4]. *Moore's law* is also expected to break down in the coming years [5], which will mean the end of the advancements of this particular technology. These challenges have led to research efforts in new types of technologies with the possibility of providing new digital components with higher density of computing and lower power requirements, as a replacement, or addition, to the MOSFET IC which are dominant today.

One of the alternatives to the MOSFET integrated circuit technology, is the field of spin transport electronics, or *Spintronics*. This field differs from traditional electronics in that it seeks to utilize the intrinsic spin of electrons, instead of just the charge. The additional degree of freedom offers the possibility to achieve higher density of data storage and transfer with higher energy efficiency. Two spintronics components are already used for data storage today: hard disk drive (HDD) and random access memory (RAM). They utilize the discoveries of the tunnel magnetoresistance (TMR) and the giant magnetoresistance (GMR), which made it possible to read data from the magnetization of materials by using electrical resistance, while external magnetic fields were used to write the data [6]. Another discovery in this field that opens a lot of opportunities is spin transfer torque (STT). STT uses spin-polarized currents to toggle the magnetization in a material, instead of external magnetic fields. This approach is anticipated to require less energy, and simplifies the memory cell design. A new type of spintronic-based data storage system was proposed in 2008 by Parkin et al. [1] from IBM, and is called racetrack memory. This technology encodes data on a "racetrack", with magnetic domain walls or other magnetic topological solitons, which can be moved along the racetrack over read and write elements using STT. Racetrack memory has the potential of providing faster read/write time than RAM, while being non-volatile.

One such magnetic topological soliton, first theoretically predicted in 1989 by A. Bogdanov and D. Yablonskiui [7], is called *magnetic skyrmions*. They are based on the more general idea of skyrmions, which were discovered by Tony Skyrme [8]. Magentic skyrmions have recently increasingly been regarded as a promising candidate for encoding data, both for storage as well as for transfer. What makes them especially attractive for spintronic applications, is their topological nature. Firstly, they are believed to be stable in a condensed matter system, because of topological protection. Secondly, skyrmions can exist on nanometer scales, which opens the possibility for high information density. And lastly, they have been shown to couple strongly with spin-polarized current, which means they can be moved rapidly using STT. The first skyrmions that were experimentally observed were in the chiral itinerant-electron magnet MnSi in 2009 [9]. Later, in 2017, magnetic skyrmionic bubbles in room temperature were observed experimentally in a frustrated kagome ferromagnet Fe_3Sn_2 [10]. And as of today, Fe_3Sn_2, and the Kagome system it is a part of, remains one of the most promising candidates for the realization of skyrmions. Most of the research that has been conducted on Fe_3Sn_2 has been on bulk crystal materials. However, for the desired spintronic applications of magnetic skyrmions, it is necessary to study thin film crystals. The first attempts at growing thin films of this Kagome magnet system, was on FeSn by Inoue et al. in 2019 [11].

Molecular beam epitaxy (MBE) is an epitaxial growth technique which can be used to deposit high crystalline thin films. It has been used to manufacture MOSFETs and diodes, among other things, for many years [12], and is also widEly used in the research and development of new nanotechnological components. This work will utilize MBE in order to grow thin films of the Kagome magnet system Fe-Sn. The focus will be two-fold: First, the growth of stable single-phase films, consisting of a Kagome lattice structure. The second focus will be to achieve the growth of large crystallites, and eventually continuous 2-dimensional crystal growth. This work is a continuation of my specialization project, and will is conducted in collaboration with the MBE Group from the Center for Quantum Spintronics, Department of Physics, Norwegian University of Science and Technology (NTNU).

Chapter 2

Background

2.1 Magnetism

2.1.1 Micromagnetic model

The source of all magnetic effects is the microscopic properties of the electron. All electrons carry a magnetic moment, which can be split into two parts

$$\boldsymbol{\mu} = \boldsymbol{\mu}_{spin} + \boldsymbol{\mu}_{orbit}, \tag{2.1}$$

where $\boldsymbol{\mu}_{spin}$ is the intrinsic magnetic moment of the electron, originating from the spin. $\boldsymbol{\mu}_{orbit}$ is the component which emerges from the orbital motion of the electron in an atom, while $\boldsymbol{\mu}$ is the total magnetic moment.

In magnetic materials, it is often useful to look at the *magnetization*, **M**. Magnetization is the volume density of magnetic dipole moments. It is a continuous vector field, however it can be approximated from the discrete magnetic dipole moments [13]

$$\boldsymbol{M} = \lim_{\Delta V \to \{p\}} \frac{1}{\Delta V} \sum_{k=1}^{n\Delta V} \boldsymbol{\mu}_k, \tag{2.2}$$

where **M** is the magnetization, ΔV is a volume which approaches a point p, and n is the number of atoms per volume.

2.1.2 Magnetic domains

Magnetic domains are regions in magnetic materials where the magnetization is uniform. The details of the domain walls differ between ferromagnetic and antiferromagnetic materials, because of the way neighboring magnetic moments align. A magnetic material typically consists of multiple magnetic domains, and the region between two domains where the magnetization gradually switch direction is called a domain wall. There exists two types of domain walls; Bloch walls and Néel walls. The difference between the two is the direction in which the magnetization rotate over the domain wall, in a Bloch wall the rotation is about an axis normal to the domain wall, while in a Néel wall the axis of rotation is orthogonal to the domain wall. In addition to these standard domains structures, more interesting topological soltions can also exist in the magnetization of a crystal, which will be discussed in more detail later.

According to micromagnetics and domain theory [14], the specific domain structures present in a material depends on the total free energy of the system. The magnetization density in any particular region is such that the free energy is in a global or local minimum. The total magnetic free energy is comprised of different magnetic exchange interactions, and the relationship between these decides the magnetic domains. These exchange interactions can either be local or non-local. Local interactions are based on the energy densities, or the local magentization, within the material, while non-local interactions are due to external factors, for example an external magnetic field. Because of the energy dependence of magnetic domains, they can only be permanently present below certain characteristic energy levels, or temperatures. The critical temperatures for ferromagnets are called the *Curie temperature*, T_C, while for antiferromagnets they are called *Néel temperature*, T_N. Above these temperatures the magnetic moments become disordered, as long as no non-local interactions are present. However, magnetism may still be induced by external fields, as in the case of paramagnetic and diamagnetic materials.

For the next section, the total magnetic free energy will be separated into five terms, and can be expressed as an effective hamiltonian $\hat{H}$:

$$\hat{H} = \hat{H}_{dd} + \hat{H}_{exch} + \hat{H}_{DMI} + \hat{H}_{anis} + \hat{H}_{Z}, \tag{2.3}$$

where $\hat{H}_{dd,ij}$ is the Dipole-dipole/demagnetization interaction, $\hat{H}_{exch}$ is the Heisenberg exchange interaction, $\hat{H}_{DMI}$ is the Dzyaloshinskii-Moriya interaction, $\hat{H}_{anis}$ is the magnetocrystalline anisotropy interaction, and $\hat{H}_Z$ is the Zeeman interaction. Each of these components will be explained in more detail in the following section.

2.1.3 Magnetic exchange interactions

Dipole-dipole/demagnetization interaction

Dipole-dipole interaction is the direct magnetic interaction between two magnetic dipole moments. Given two spins in a material, $\mathbf{S}_i$ and $\mathbf{S}_j$, with corresponding positions, $\mathbf{R}_i$ and $\mathbf{R}_j$. $\mathbf{S}_j$ creates a long-range magnetic field, which $\mathbf{S}_i$ couples with. The strength of the interaction depends on both the distance between the dipoles, as well as their relative orientation. Summing over all i's and j's, the total energy of this interaction can be expressed as the hamiltonian [15]

$$\hat{H}_{dd} = \frac{\mu_0}{2\pi} \frac{\mu_B^2}{\hbar^2 |\mathbf{R}_i - \mathbf{R}_j|^3} \left[\mathbf{S}_i \cdot \mathbf{S}_j - 3(\mathbf{S}_i \cdot \mathbf{e}_{ij})(\mathbf{S}_j \cdot \mathbf{e}_{ij}) \right] \tag{2.4}$$

with

$$\mathbf{e}_{ij} = \frac{\mathbf{R}_i - \mathbf{R}_j}{|\mathbf{R}_i - \mathbf{R}_j|}, \tag{2.5}$$

where μ_0 is the magnetic permeability in vacuum, and μ_B is the Bohr magneton. This is typically one of the dominating interactions in the formation of magnetic domains. If one starts with a single-domain material, with all magnetic moments aligned, one will have a large magnetic field extending outside of the material. This requires a lot of magnetostatic energy. To reduce the energy, the system tends to be split into multiple smaller domains with magnetization on opposing directions. This reduces the total net magnetization of the material, and is why this interaction is commonly called *the demagnetization interaction.*

Heisenberg exchange interaction

The Heisenberg exchange interaction is a purely quantum mechanical effect, which results in an apparent exchange force between two identical spins. It is caused by an exchange symmetry of the wave function of two identical particles. This means that if the two indistinguishable particles swap places, the sign of the wave function must either change (antisymmetric) or remain the same (symmetric). Exchange interactions applies to both fermions and bosons, and the effect is antisymmetric and symmetric, respectively. For fermions, the exchange interactions cause a repulsive force between identical particles, and one consequence of this is that two electrons with the same spin can not occupy the same space, which is known as the *Pauli exclusion principle.* While for bosons, the interactions causes an attraction between identical particles, like in Bose-Einstein condensates.

Although this interaction is not a real exchange force, Heisenberg made a perturbation term to the hamiltonian which encapsulates the effective force of the exchange interaction [14, 15]:

$$\hat{H}_{exch} = -\sum_{i,j} J_{ij} \mathbf{S}_i \cdot \mathbf{S}_j, \tag{2.6}$$

where J_{ij} is the exchange constant for the interaction between two spin particles $\mathbf{S}_i$ and $\mathbf{S}_j$. For a magnetic material, the Heisenberg exchange interaction mainly affects neighboring particles. And the result is a drive to align the spin of neighbouring particles, either parallel or antiparallel, depending on the sign of J_{ij}. If $J_{ij} > 0$, the material is a ferromagnet, while if $J_{ij} < 0$, it is an antiferromagnet.

Dzyaloshinskii-Moriya interaction

The Dzyaloshinskii-Moriya interaction (DMI) is an antisymmetric contribution to the exchange interaction between two spins. This effect can be expressed as a term added to the total hamiltonian:

$$\hat{H}_{DMI} = -\sum_{i,j} \mathbf{D}_{ij} \cdot \big(\mathbf{S}_i \times \mathbf{S}_j\big), \tag{2.7}$$

where $\mathbf{S}_i$ and $\mathbf{S}_j$ are two spins, and $\mathbf{D}_{ij}$ is the Moriya vector. The interaction favors canting of the atomic spins in systems that otherwise would have parallel or antiparallel spins, and can cause weak ferromagnetism in antiferromagnetic systems. DMI is fundamental to the existence of magnetic skyrmions and long-ranged helimagnetic order.

Magnetocrystalline anisotropy interaction

Magnetocrystalline anisotropy is the interaction between the spins and the underlying crystal lattice. The energy from this interaction is reduced when the magnetization is aligned in certain directions, which are typically related to the principal axes of the lattice. The main source of this effect is spin-orbit coupling [14], where the crystalline electric field affects the orbital angular momentum of the electrons, which determines the magnetic structures in the material.

Since this interaction is so dependent on the crystal structure, the details of the energy varies a lot with the class of crystal that is considered. One example is crystals with one single axis of high symmetry, which are called *uniaxial.* If the anisotropy direction $\mathbf{u}$ is parallel with $\hat{\mathbf{z}}$ in a ferromagnet, the Hamiltonian can be expressed as [15]:

$$\hat{H}_{anis,u} = -\sum_{i,j} K_{ij} S_i^z S_j^z, \tag{2.8}$$

where K_{ij} is uniaxial anisotropy constant, which depends on composition and temperature, and S_i^z and S_i^z are the components of the two spins in the $\hat{\mathbf{z}}$-direction.

Another class of crystals is those with *cubic symmetry.* For a cubic ferromagnet, the anisotropy hamiltonian is

$$\hat{H}_{anis,c} = -\sum_{i,j,k,l} \sum_{\alpha \neq \beta}^{(x,y,z)} K_{ijkl} (S_i^\alpha S_j^\alpha)(S_k^\beta S_l^\beta), \tag{2.9}$$

where K_{ijkl} is the anisotropy constant, and S_i^α is spin i in the direction α.

Zeeman interaction

The Zeeman interaction is the coupling between the spins of a crystal and and externally applied magnetic field. The energy of this interaction is reduced when the spins are aligned with the magnetic field. The hamiltonian [15] of this effect can be expressed as

$$\hat{H}_Z = -2\frac{\boldsymbol{\mu}_B}{\hbar} \sum_i \mathbf{S}_i \cdot \mathbf{B}_{ext}, \tag{2.10}$$

where $\mathbf{B}_{ext}$ is the externally applied magnetic field, and $\mathbf{S_i}$ is a spin in the crystal.

2.2 Topological solitons

Domain walls is one type of a larger class within magnetic domain structures called topological solitons. This encapsulates any configuration of a field that is different from the environment, and that can not be continuously transformed into something topologically trivial.

2.2.1 Mathematical formulation

The topological charge, or topological index, of a configuration in a field is often used to categorize topological solitions. For 2-dimensional topological solitions, this value can be expressed mathematically as [16]

$$N_{Sk} = \int n_{Sk}(\mathbf{r}) d^2 r, \tag{2.11}$$

which is an integral over the topological charge density n_{Sk}, which can be defined as

$$n_{Sk} = \frac{1}{4\pi} \mathbf{m}(\mathbf{r}) \cdot \left[\frac{\partial \mathbf{m}(\mathbf{r})}{\partial x} \times \frac{\partial \mathbf{m}(\mathbf{r})}{\partial y} \right], \tag{2.12}$$

where $\mathbf{m}(\mathbf{r})$ is the magnetization in position r. (Note that in order to apply theory from topology when discussing magnetic topological soltions, a continuous-field approximation must be made of the individual spins, to a continuous magnetization field, as described in section 3.1 with equation (2.1). This expression can be simplified and made more intuitive by applying spherical coordinates. By expressing the position as $\mathbf{r} = r(\cos\phi, \sin\phi)$, and splitting the magnetization into an azimuthal angle component $\theta(\phi)$ and the polar angle component $\Phi(\phi)$, the topological charge becomes [16]

$$\begin{aligned} N_{Sk} &= \frac{1}{4\pi} \int_0^\infty dr \int_0^{2\pi} d\phi \frac{\partial \Phi(\phi)}{\partial \phi} \frac{\partial \theta(r)}{\partial r} \sin\theta(r) \\ &= -\frac{1}{2} \cos\theta(r) \big|_{r=0}^{\infty} \cdot \frac{1}{2\pi} \Phi(\phi) \big|_{\phi=0}^{2\pi} \\ &= m \cdot p, \end{aligned} \tag{2.13}$$

where the topological charge was separated into two more intuitive factors, m and p. p is the polarity of the soliton, and can only have values $p = \pm 1$. m can be identified as the vorticity, with possible values $m = 0, \pm 1, \pm 2, ...$

This means that topological charge of a solition will be an integer value

$$N_{Sk} = \pm 1, \pm 2, ...$$

In addition to the polarity and the vorticity, a third value is used for classifying different types of skyrmions. This is the *helicity* γ, which is defined as the phase offset of the polar angle component of the magnetization density Φ, from the linear dependence of ϕ

$$\Phi = m\phi + \gamma. \tag{2.14}$$

The helicity is what distinguishes two important classes of skyrmions, *Néel skyrmions* and *Bloch skyrmions*, which both have topological charge $N_{Sk} = 1$. Néel skyrmions have helicity $\gamma = 0$, and is typically observed at interfaces of materials. The in-plane component of the magnetization of this type always points in the radial direction. On the other hand, Bloch type skyrmions have helicity $\gamma = \pm\frac{\pi}{2}$, and has magnetization perpendicular to the position vector.

2.2.2 Magnetic skyrmions

The micromagnetic source of the different types of skyrmions can vary from material to material, based on which interaction is dominant. The most typical source of stability of skyrmions is the Dzyaloshinskii-Moriya interaction, competing with the Heisenberg exchange interaction which promotes ferromagnetic order. This can be responsible for a variety of different types of skyrmions, such as Néel type, Bloch type and antiskyrmions, among others [16]. Another possible source of stability for skyrmions is dipole-dipole interactions. Compared to skyrmions protected with DMI, the dipole-dipole interaction can stabilize larger solitons, up to several micrometers in diameter.

2.3 The Kagome magnet system Fe-Sn

The Kagome magnet system Fe-Sn is a set of crystals consisting of stacked layers of Fe_3Sn and Sn_2. Fe_3Sn is a two-dimensional Kagome net, composed of equilateral triangles of Fe-atoms structured such that they share corners. The triangle-sharing net leaves hexagonally shaped vacancies, which are filled with single Sn-atoms. The two-dimensional honeycomb spacing layer Sn_2 separates the Kagome layers. The stacking sequence of the two layers can be varied to reveal different topological phases, with different exotic properties.

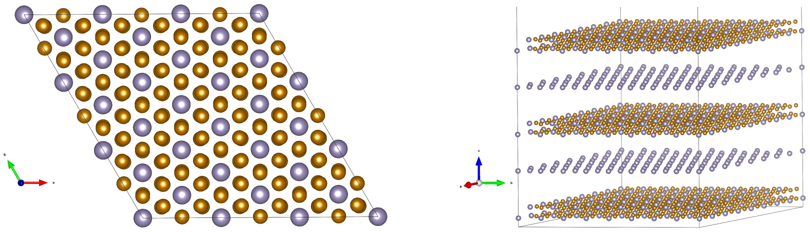

(a) Top view (xy-plane) of the Kagome layer.

(b) Side view (xyz-plane), showing the stacking of bilayers of Fe_3Sn_2 and single layers of Sn_2.

Figure 2.1: Schematic of the crystal structure of Fe_3Sn_2.

2.3.1 Fe_3Sn_2

The most studied phase of this system is Fe_3Sn_2. This consists of offset bilayers of Fe_3Sn and Sn_2 separated by a single layer of Sn_2. Fe_3Sn_2 has a centrosymmetric crystal structure and is in the rhombohedral space group $R\bar{3}m$. The lattice parameters for the crystal are $a = b = 5.3145$Å and $c = 19.7025$Å [17], for the tripled hexagonal unit cell where a and b are along the layers and c is in the stacking direction. It is a non-collinear frustrated ferromagnet with Curie temperature of $T_C = 640$K. Fe_3Sn_2 was first numerically predicted to host stable skyrmions at room temperature in 2014 by Pereiro et al. [18]. Then, in 2017, Hou et al. [10] made experimental observations of skyrmionic bubbles in Fe_3Sn_2 at room temperature. They attributed the stability of the skyrmions to be the magnetocrystalline uniaxial anisoptopy (see section 2.1.3).

Fe_3Sn_2 has been identified as a frustrated itinerant ferromagnet, and has been found to have other exotic properties [17]. For instance, a low-temperature spin glass phase below 80K, as well as an unusually large anomalous Hall effect [19]. Additionally, quasi-two-dimensional Dirac cones were observed in 2018 [20], and in 2019, the system was shown to have Dirac fermions with intrinsic spin-orbit coupling in the d electron sector [21].

2.3.2 FeSn

Another interesting topological phase of the Fe-Sn Kagome system is FeSn. This crystal consists of a single layer of Fe_3Sn, separated by a single layer of Sn_2. It is antiferromagnetic and has a critical temperature of $T_N = 353$K. FeSn has been predicted to host Dirac fermions in its electronic structure. The first attempt at growing thin film single crystalline FeSn using epitaxy was made by Inoue et al. in 2019 [11].

Most of the experiments that has been conducted on this Kagome magnet system so far, has been on bulk crystals. However, in order to achieve applications in spintronic components, it is advantageous to study the properties of single crystalline thin films.

Chapter 3

Molecular beam epitaxy

In this work, thin films of iron (Fe) and tin (Sn) are grown using epitaxial methods with the goal of achieving the Kagome structures presented in the previous chapter. This chapter introduces molecular beam epitaxy (MBE), which is the growth method that is used in order to synthesize the thin films. MBE is used in both research as well as in industry, for the production of electronic and optical devices where the crystal structures are complicated and the quality requirements are high.

The technical working principles of the device are presented in detail below, with focus on key parameters which affect the growth. Parts of the technical working principles are centered around the specific device which was used in this project.

3.1 Main components

The basic principle of MBE is to deposit molecules onto a substrate using molecular beams, which then form new crystals. The main components of a typical MBE device are Knudsen cells which contain the materials and create the gaseous beams, and a substrate on the receiving end of the beams. Additional components can also be utilized, such as in-situ reflective high-energy electron diffraction (RHEED), which will be discussed more detail in the next chapter (see section 4.1). All components are enclosed in a ultra-high vacuum chamber. A schematic overview can be seen in figure 3.1.

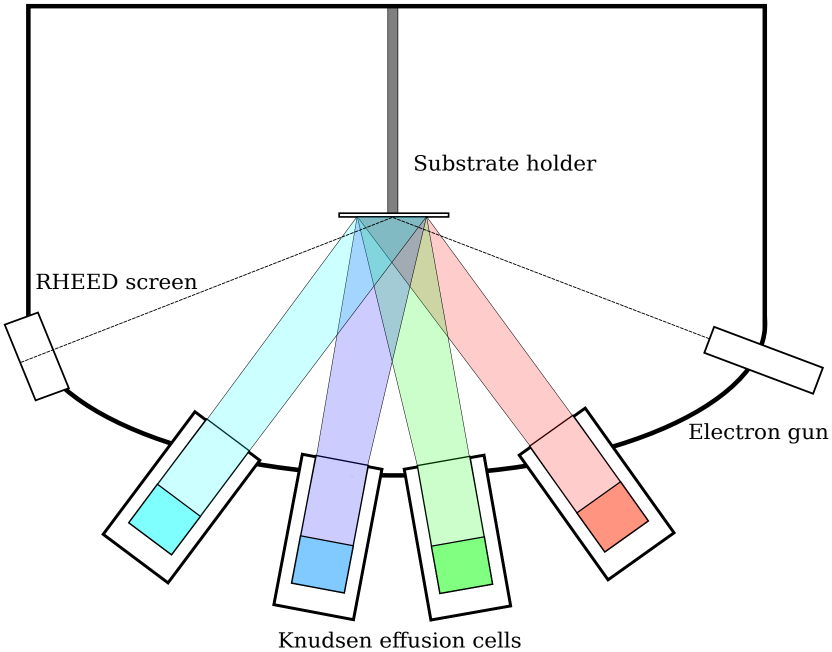

Figure 3.1: Schematic of a MBE chamber showing the substrate holder, effusion cells and the RHEED system.

3.2 Ultra-high vacuum

Ultra-high vacuum (UHV) is defined as pressures below 10^{-8} Torr [22], which is equivalent to 10^{-11}bar. At these levels, the mean free path of the gas molecules is greater than 5.1km, which means that the Knudsen number $Kn > 10$ [23] for the dimensions of a MBE chamber, and the gas is in a state of free molecular flow. UHV is necessary for MBE growth in order to avoid contamination of other molecules in the new crystals. This would change the constituents of the crystal structure and decrease the purity of the crystal, as well as negatively affecting the surface morphology of the growth [24]. Additionally, UHV opens the possibility of decreasing the deposition rate and subsequent growth rate significantly, which adds a degree of freedom to the growth.

To reach these pressures practically, the rate of inflow and outflow of gases must be balanced correctly. The inflow is reduced by enclosing all components in a specially designed steel chamber. Stainless steel is beneficial for this purpose, because it is strong enough to withstand the pressure differences as well as having low out-gassing on the inside of the chamber. The main source of leaks are in the flanges, where different steel components need to be connected. Copper gaskets are placed in the flanges, and compressed on a knives edge, in order to tighten the gap. The steel chamber typically has double-walled cooling shroud inside of the vacuum walls, which can be filled with liquid nitrogen. This makes the walls of the inside of the chamber cold enough that gas molecules condense on the surface, which helps reduce the pressure further.

The outflow of gas from the chamber is maximized by using a set of pumps with different working principles. Some of the pumps work in different pressure ranges, so that they together can operate from atmosphere pressures and down to UHV. A root vacuum pump can be used from 1 atmosphere (760 Torr) to around $7.5 \cdot 10^{-3}$ Torr [25], but also as a backing pump for the other pumps. Between around 1 Torr and 10^{-8} Torr, a turbomolecular pump is used. A turbomolecular pumps works by transferring momentum to the gas molecules by repeated collision with rotating blades. For the operating pressures of $< 10^{-8}$ Torr, two pumps are used in the MBE machine in this project: a cryogenic pump and an ion-getter pump. The cryogenic pump, or cryopump, functions by condensing gas molecules onto a cold head, which is cooled typically by H_2 gas. It can have multiple steps of different temperatures aimed at different molecules [26]. The ion pump ionizes gas molecules with electrons, typically with a penning trap. The ionized molecules are accelerated via an electric or magnetic field towards a chemically active cathode, where they condense [27].

3.3 Vapor pressure

One of the key parameters affecting the growth is the *vapor pressure*, and the *flux ratio*. Vapor pressure is the pressure of the molecular beam from each of the Knudsen cells. It directly affects the deposition rate of that specific molecule onto the substrate, and together with the sticking coefficient controlled largely by the substrate temperature, determines the growth rate. The relationship between the vapor pressure and the substrate temperature will be discussed more in the following subsection. Related to the vapor pressure is the flux rate, which is a measure of the number of atoms per area per second in the molecular beam. If more than one material is used, the *flux ratio*, or stoichiometric ratio, is important. This is the relationship between the flux rates of the different atoms, and needs to be equal to the composition of the crystal that is grown.

The evaporation rate, or sublimation, of a solid depends on the temperature. Knudsen cells control the vapor pressure by controlling the temperature of the material inside. The relationship between the temperature of a solid or a liquid and the vapor pressure is captured by the empirical equation from the producers of the MBE evaporation cells used in this work, MBE Komponenten [28]:

$$p = 10^{A-B/T}, \tag{3.1}$$

where A and B are material-specific coefficients, T is the temperature in Kelvin, while p is pressure in unit millibar (mbar). Inserting the empirical coefficients given by MBE Komponenten for iron [29] and tin [30], we get

$$p_{\mathrm{Fe}} = 10^{10.353-21038/T}, \tag{3.2}$$

and

$$p_{\mathrm{Sn}} = 10^{8.266-15415/T}. \tag{3.3}$$

The flux of particles in the molecular beams can be related to the pressures by using the relation

$$\Phi = \frac{p}{m \cdot v}, \tag{3.4}$$

where m is the mass of the particles, v is their velocities, and Φ is the particle flux. The velocity can be estimated by using the average velocity of particles in a gas with a known temperature, as known from the kinematic theory of gases:

$$\frac{1}{2}m\bar{v}^2 = \frac{3}{2}k_{\mathrm{B}}T \quad \rightarrow \quad m\bar{v} = \sqrt{3k_{\mathrm{B}}Tm}. \tag{3.5}$$

This gives the flux

$$\Phi = \frac{p}{\sqrt{3k_B Tm}}. \tag{3.6}$$

The flux ratio between Fe and Sn can then be expressed as

$$\kappa = \frac{\Phi_{\mathrm{Fe}}}{\Phi_{\mathrm{Sn}}} = \frac{p_{\mathrm{Fe}}/\sqrt{T_{\mathrm{Fe}}m_{\mathrm{Fe}}}}{p_{\mathrm{Sn}}/\sqrt{T_{\mathrm{Sn}}m_{\mathrm{Sn}}}} \tag{3.7}$$

with p_{Fe} and p_{Sn} defined in 3.2 and 3.3. However, this is the theoretical vapor pressure and flux directly from the source of sublimation. The real values of the flux hitting the substrate surface will be significantly reduced. First, the molecular beams will have a non-zero angle of incidence, which may differ between the different cells. A second factor is the angular distribution of the molecular beam itself, which determines how much the flux dissipates over distance. This is largely determined by the shape of the crucible, and especially the dimension of the orifice, relative to the target substrate. These factors deviating the theoretical values from the real values, makes it necessary to determine the deposition rate experimentally, in order to grow with a correct flux rate and flux ratio.

The stoichiometric composition of the $\mathrm{Fe_3Sn_2}$ crystal is 3 iron atoms per 2 tin atoms. Therefore, the ratio of (Fe:sn) that is incorporated into the crystal, must be 3:2. However, the materials will experience different sticking coefficients and surface chemistry, among other factors. This means that if a constant flux is applied, the flux ratios in the molecular beams will not necessarily be identical to the stoichiometric composition of 3:2. Additionally, alternative growth techniques may be applied which changes the ratio. A separate material can be grown before or after the desired crystal, either as a buffer layer between the substrate and the crystal as demonstrated by Cheng et al. [31], or as a protective layer like Inoue et al. [11]. Bilayered structures like the Kagome system Fe-Sn can also be grown layer-by-layer. This technique used by Cheng et al. grows layers of $\mathrm{Fe_3Sn}$ and $\mathrm{Sn_2}$ sequentially by changing the stoichiometric flux ratios after each new layer. This method requires accurate control of the cell shutters as well as accurate reading of the growth rate [32].

3.4 Nucleation and surface diffusion

When molecules from the molecular beams land on the surface of the substrate, they will either be incorporated into the substrate or re-evaporate from the surface. The ratio of atoms that are incorporated into the crystal is called the *sticking coefficient*. The sticking coefficient depends on the materials in the molecular beam, the substrate material and temperatures, among other factors. The value of the sticking coefficient is typically too complex to calculate theoretically, and is therefore mostly determined experimentally. The sticking coefficient, in combination with the total flux of the molecular beams incident on the substrate, determines the growth rate.

However, before being incorporated or re-evaporated, the adsorbed atoms, or *adatoms*, migrate across the surface of the crystal. The average distance the adatoms migrate is called the surface diffusion length, and can be defined separately for incorporation and re-evaporation [33]. The incorporation diffusion length is an important parameter affecting the growth during MBE. In order to achieve layer-by-layer 2D crystal growth, the incorporation diffusion length needs to be long enough that the adatoms can reach the edge of the new developing layer. If this diffusion length is too short, the adatoms will nucleate in different spots, which creates 3D structures on the surface, such as crystal islands.

During MBE, there are three main modes of growth: amorphous, three-dimensional and two-dimensional. Amorphous materials have no crystalline structure, and are not relevant to this work. Fe_3Sn_2 may be grown as either three-dimensional or two-dimensional materials, however two-dimensional growth is strongly preferred for the thin films this work aims to synthesize. In-situ characterizations of the growth can be done with RHEED (section 4.1) in order to determine which mode of is present. One typical three-dimensional structure which is often observed is separated crystal islands.

Additionally, the choice of substrate material and crystal structure is also an important factor for the growth. There may be cross-reactions between the material of the substrate and one or more of the materials from the molecular beams, which create unwanted materials. If the cross-reaction dominates over the crystal one wish to grow, it will hinder the growth of the desired crystal.

The lattice constants parameters of the substrate may also determine which crystal structures that are able to grow. Specifically the lattice matching between the growing crystal and the substrate. From section 2.3.1 we know that the lattice parameters of Fe_3Sn_2 are $a = b = 5.3145$Å and $c = 19.7025$Å. A bad/low lattice matching leads to Asaro–Tiller–Grinfeld instability (ATG) [34], which is the build-up of elastic energy in the growing film. This can lead to the crystal breaking into separated crystal islands at a certain critical thickness.

Chapter 4

Characterization techniques

This chapter presents the techniques that are used in this work to characterize the samples grown with MBE. The different measurements give different insights into the film that is grown. And the results from the measurements are used to guide the search in parameter space in order to achieve the correct crystal structures, as well as to optimize the film quality. The first type of measurement is done in-situ, during the growth, with reflection high-energy electron diffraction (RHEED). All the other characterizations are made after the growth, on the finished sample. The most important ones used are X-ray diffraction (XRD) and scanning electron microscopy (SEM), which give detailed insights into the crystal structure and the surface topology. Energy-dispersive X-ray spectroscopy (EDS) is also commonly used for elemental analysis. Based on the results from the prior measurements, further characterization techniques can be used, including atomic force microscopy (AFM) for very high resolution imaging of the surface topology and magnetic force microscopy (MFM) for the magnetic structures on the surface. The following sections gives a more detailed explanation of the technical details of RHEED, XRD, SEM and EDS.

4.1 Reflection high-energy electron diffraction

In situ reflection high-energy electron diffraction (RHEED) is used to monitor the sample during growth. For a RHEED setup, an electron gun is located on on side of the main chamber, shooting electrons with energies in the range of $2-50$keV [35]. The electrons pass through an aperture and are focused by a magnetic focusing lens. The electron beam is deflected in such a way that it reflects off the sample surface with a small glancing angle (θ_g) of around $0.5^\circ - 6^\circ$ [36], and hits a fluorescent on the opposite side of the chamber. A schematic of the electron gun and the fluorescent screen can be seen in figure 3.1. The focusing lens is adjusted so that the focused spot on the screen is less that 0.1mm [36]. The main advantage of RHEED is the small glancing angle, which means that no components of RHEED measurements interferes with the evaporation beams from below the substrate, or the substrate holder from directly above the substrate. This in turn means that the measurements can be done continuously throughout the growth, by observing the diffraction pattern on the fluorescent screen.

The diffraction pattern observed on the fluorescent screen can be understood intuitively with the *Ewald sphere construction.* The momenta of the incident, as well as scattered, electrons can be presented as an Ewald sphere, as long as only elastic scattering is considered. An Ewald sphere is a sphere in reciprocal space, created by k-vectors (wave vectors) of equal length, originating from the same point. The diffraction pattern is the intersection between the Ewald sphere, and the reciprocal lattice of the crystal [36]. For an ideal perfect flat surface of a single-crystalline material, the electron beam only scatters off the top layer. The diffraction pattern from a 2D square lattice consists of spots which can be divided into groups of concentric circles, called *Laue zones.* However, in reality, the beam penetrates the bulk crystal, which can cause additional diffraction spots or patterns.

In practice, RHEED can be utilized to distinguish different types of crystal surface morphology during MBE growth. Hasegawa [36] presents various kinds of realistic growth modes, comparing the real-space morphology to the corresponding RHEED pattern. The most important of these growth modes are presented in figure 4.1.

When the real-space surface is atomically flat and single-crystalline, the reciprocal space (for only the top layer) becomes thin sharp rods. And the intersection with the Ewald sphere gives a RHEED pattern consisting of sharp dots, only on the Laue zones. However, with interference from electrons that penetrate deeper layers of the crystal, the intensity of the rods varies which causes some variation of the intensity of the diffraction spots.

Another useful example is the case of an atomically flat poly-crystalline surface, consisting of small domains of out-of-phase crystals. Compared to the last example, the rods in reciprocal space for this system are broader. This causes elongated streaks in the diffraction pattern, instead of spots. The width of the rods are inversely proportional to the average size of the crystal domains, and can be used as an advanced technique to estimate the average size of the domains. A third example is the case of a more rough crystal surface with 3D islands. In this case, the electron beam will transmit through the bulk crystal, and the reciprocal space will consist of many points, which is consistent transmission diffraction rather than reflection diffraction. The resulting diffraction pattern will be lots of transmission spots, located around the Laue zones [36] [35].

Distinguishing between diffraction dots and streaks in the RHEED measurements, and relating them to 3D growth and 2D growth, respectively, has been used in MBE research for decades [35]. Combining in-situ RHEED measurements with MBE growth was first studied by Alfred Y. Cho et al. in a series of studies 1969-1975 ([37], [38], [39], [40], [41], [42], [43]). In a paper by A. Y. Cho and J. R. Arthur from 1975 [43], images of RHEED diffraction patterns and electron microscope topology were compared for multiple samples with different

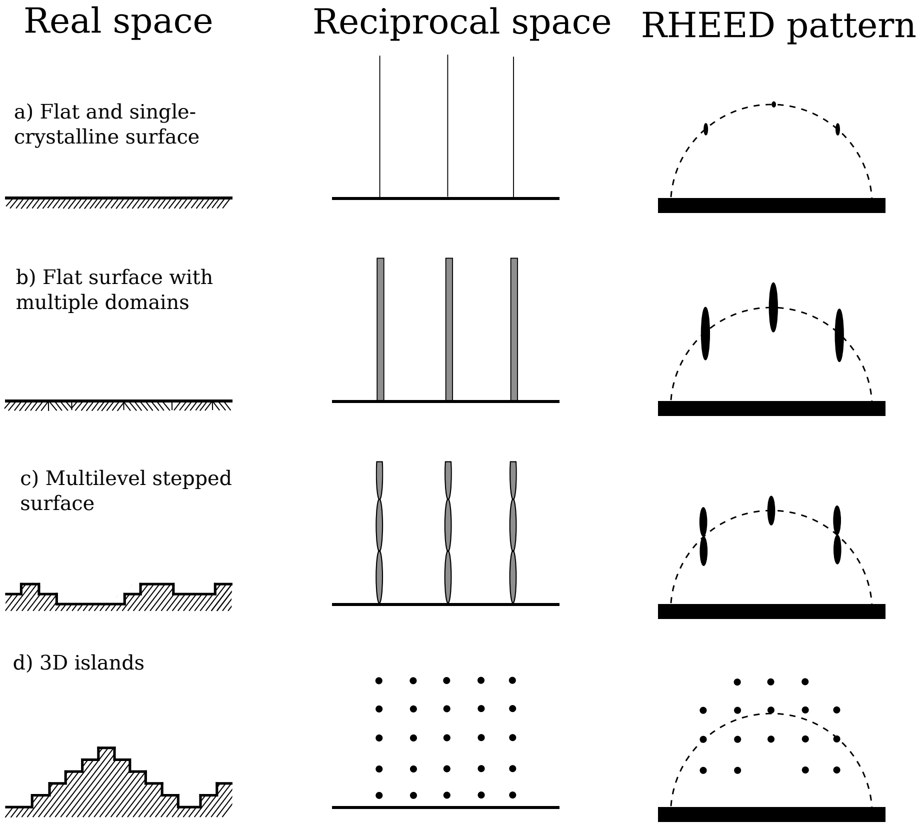

Figure 4.1: Realistic growth modes in real space, reciprocal space and the resulting RHEED patterns, adapted from [36].

surface roughness. A correlation between streaks in the RHEED pattern and less surface roughness/more atomically flat was found.

The intensity of the diffraction patterns on the fluorescent screen oscillates during growth. The oscillations have been found to correlate with the deposition rate during layer-by-layer MBE growth, with the periods of the oscillations corresponding to the deposition time for each monolayer [44]. This makes it possible to calculate the thickness of a sample, by measuring and counting the number of deposited monolayers. However, this technique is not used for this work. Instead, the thickness is estimated by cross-sectional SEM images, although, the uncertainty in this technique is significantly larger, comparatively.

The origins of these oscillations have been studied extensively, but are still not understood completely. However, calculations of the RHEED intensity distributions calculated from the wave function inside and outside the crystal surface has revealed that there are only two possible origins for the intensity oscillations [45]. The first is the interference between waves diffracted by the top layer, and the underlying layers. The other is the disturbance of the RHEED diffraction pattern by step edges.

4.2 X-ray diffraction

X-ray diffraction (XRD) measurements are done post growth, and are used to analyze and classify the crystal structure of the sample. With the materials deposited, iron and tin, in addition with the substrate itself, a large variety of different crystal structures may be grown. XRD is used to classify these, and especially to detect if Fe_3Sn_2 growth is achieved.

For an XRD measurement, the thin film sample is placed on a goniometer which allows for precise rotation of the sample. On one side of the sample is an x-ray source, while on the other is a detector, both of which can rotate relative to the sample. A schematic view of the setup is included in figure 4.2.

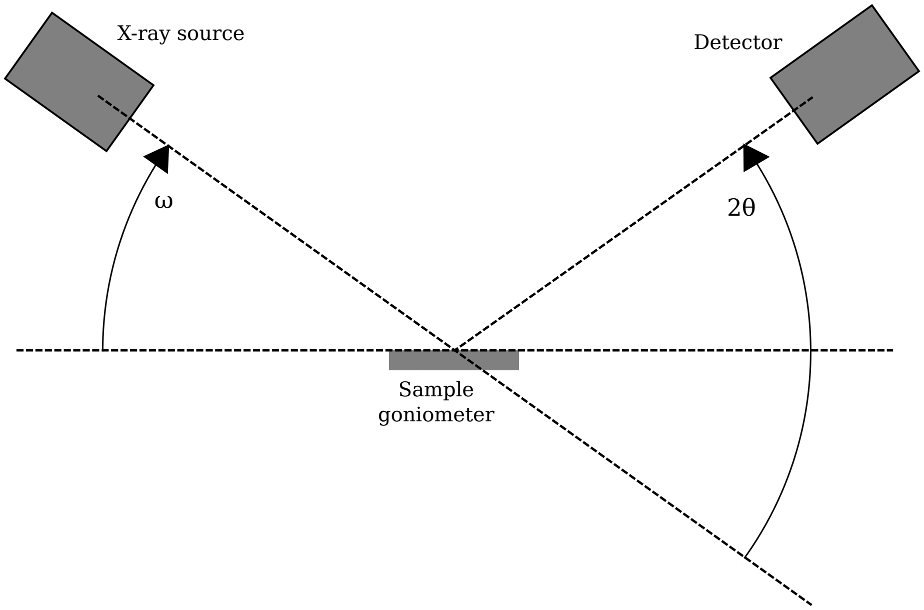

Figure 4.2: Schematic of a XRD instrument, showing the sample, an X-ray source and a detector, with relevant angles.

The x-ray beam hits the sample with an incidence angle ω, and the diffracted beam is detected from an angle 2θ, relative to ω. Additionally, the azimuthal angle of rotation of the sample is typically denoted as ϕ. A variety of different measurements can be conducted, by continuously changing or fixing different sets of these angles. The type of measurement that will be used the most in this work, is a symmetric $2\theta/\omega$-scan ($\frac{2\theta}{\omega}$-scan), where ϕ is kept constant while ω is always half of 2θ, and the intensity is plotted as a function of 2θ. The physics behind this type of diffraction measurement can be explained by the elastic (Thomson) scattering of photons, which allows for the assumption of specular reflection and to treat the atomic planes as effective mirrors [46]. In addition, the distances between the atomic planes is on the same order of magnitude as the wavelengths of the X-ray beams, meaning that beams reflecting off neighboring planes will interfere constructively or destructively with each other. The angles of constructive interference for a particular interplaner distance in a crystal is expressed in Bragg's law [47]

$$n\lambda = 2d\sin(\theta), \tag{4.1}$$

where n is the diffraction order, λ is the wavelength of the X-ray beam, d is the interplanar distance and θ is the incidence angle of the beam as defined above. The possible values for d are defined by the dimensions of the unit cell in the crystal. This is why XRD is particularly useful in identifying and analyzing crystals, because it reveals details about the specific chemistry and atomic structures present in the sample. During XRD, the intensity of the diffracted beam is recorded over different θ values by rotating the sample on a goniometer. The diffraction intensity can then be plotted against θ, revealing peaks corresponding to specific crystal planes of specific materials.

Phases with known 2θ positions are used as a reference to identify the experimental peaks. The process of correlating a peak to a known crystal phase is typically called peak fitting, or indexing. The experimental peaks should match the reference values in both 2θ positions and relative intensities, however, small offsets in the experimental values can occur, which introduces uncertainties and complicates the indexing. One possible reason for offset in the measurements is specimen displacement error. This is caused by a misalignment of the sample, which leads a systematic error in the positions of the peaks. Another possible reason for shifted peak positions is strain in the crystal structures caused by a mismatch in the lattice constants of the substrate and the grown crystal (see ATG, section 3.4). Additionally, if multiple peaks are close to each other, they can appear as a single broad peak instead of smaller independent ones.

In some cases, it can be difficult to correctly index all the peaks from an XRD measurement. Especially if there are many possible reference phases with peak positions in a close range, combined with offset or merged measured peaks. In order to reduce the number of possible crystal phases a single peak can be fitted to, one typically only compare with crystal phases from combinations of the materials used for the growth. For this work, this is iron (Fe) and tin (Sn), and the materials used in the substrate.

4.3 Scanning electron microscopy

Scanning electron microscopy (SEM) measurements are used to obtain details about the surface topography and chemical composition of the sample. The measurements are done in a separate chamber post growth. The results from SEM measurements are analyzed mostly qualitatively, and can show whether the thin films consist of atomically flat single-crystalline surfaces, which is the goal of this project, or other unwanted 3D structures. Additionally, details about the crystal structures can be observed, such as their sizes and orientations. SEM is typically paired with measurements of the crystallography of the sample, such as XRD, in order to show both which crystal structures are present, and if the growth is 2D.

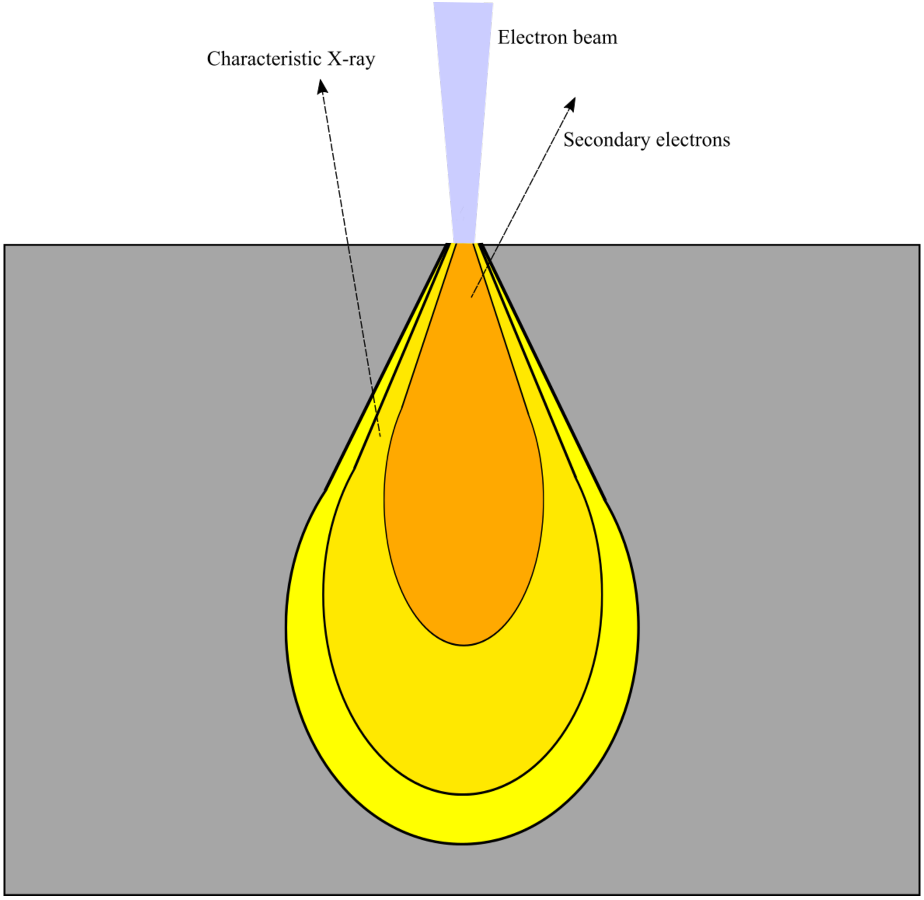

Figure 4.3: Schematic of the interaction volume from an electron beam in a crystal. Showing two characteristic signals, which are used in SEM and EDS measurements.

During the measurements, a beam of electrons are sent towards the surface of the sample, as is shown in the schematic figure 4.3. The electrons interact with a the atoms in the crystal, which gets excited, and can emit a variety of signals. The volume of the crystal the electron beams interact with, is called the *interaction volume*. The different signals emitted from the interaction volume are used for different types of measurements. The signal used for the surface topology SEM measurements are called secondary electrons, which are electrons that are emitted because of the ionization caused by the beam of electrons. The secondary electrons have energies on the order of 50eV, which is low enough that only those originating from the atoms near the surface will escape the material. The electrons are then detected, and an image is constructed by scanning the surface.

4.4 Energy-dispersive X-ray spectroscopy

The other signals emitted by the atoms in the interaction volume under an electron beam, can be used for different measurements. For instance, when the atoms absorb and emit the electrons, they emit X-ray photons 4.3. These signals are used in energy-dispersive X-ray spectroscopy (EDS).

The emitted X-ray beams are characteristic for each element, because all elements has unique atomic structures and resulting emission spectra. EDS measures the frequencies of the X-rays emitted from the scanned area, and can show the chemical composition of the sample.

EDS measurements are a quantitative measure, and shows the composition as percentages of the different elements. For this work, the results of this measurement can be used to correct the flux ratio of the Fe cell and the Sn cell.

Chapter 5

Results and discussions

This work attempts to grow thin films of the Kagome magnet system Fe-Sn using molecular beam epitaxy. The goal is to achieve single-crystalline 2D growth of the Fe_3Sn_2 structure. In order to do that, multiple samples were grown on silicon (111) and gallium arsenide (111) substrates, using different parameters. The (111) orientation is the hexagonal surface of the Si and GaAs substrates, which is used in order to fit the hexagonal plane of Fe_3Sn_2 onto the substrate.

The main parameters that were set were the growth time, the substrate temperature, and the temperatures of the Knudsen cells containing iron and tin. In order to isolate and study the effect of a single growth parameter, one parameter was adjusted methodically, while the others were kept unchanged. Each series of parameter change was guided by the results from the previous samples. The results from the relevant growth series are presented in this chapter.

The properties of the samples are first analyzed post-growth using XRD, to determine the crystal structure of the samples. The peaks are indexed by comparing the observed peaks with calculated diffraction patterns from MaterialsProject and with OriginLab software. SEM measurements are included to study the surface topology and morphology of the different samples. The SEM measurements were repeated with multiple magnifications, however for the analysis below, only measurements using the same magnification are included, in order to easier compare the samples, and show the changes. In addition, the RHEED diffraction pattern was recorded during growth for all the samples. Video stills from the recordings are included, and analyzed qualitatively.

The results can be split into two parts. The first includes the growth series conducted with silicon substrates, and the next is all the growth series on gallium arsenide substrates.

5.1 Silicon substrate

Table 5.1: Values for the growth parameters for each sample grown on Si(111) substrates.

Name	Growth time (minutes)	$T_{\text{Substrate}}$ (°C)	T_{Fe} (°C)	T_{Sn} (°C)
Sample 1	50	400	1417	1095
Sample 2	50	450	1417	1095
Sample 3	52	500	1417	1095
Sample 4	50	550	1417	1095
Sample 5	50	600	1417	1095
Sample 6	50	650	1417	1095
Sample 7	60	650	1417	1095
Sample 8	120	650	1417	1095
Sample 9	180	650	1417	1095

This section contains the relevant the growth series grown on silicon substrates, with orientation (111). The first part explores the effect of the substrate temperature during the growth. And the second part studies the effect of growth time.

All the relevant parameters for the samples in these series are presented in table 5.1. Silicon substrates were used because they are cheap, have high quality and integrate well with existing technology. Additionally, silicon has very little impurities in the lattice, and has no possible stochiometric imbalances. The fluxes were unchanged for all the samples in this part, so that the effect substrate temperature and growth time could be isolated. The values for the cell temperatures were decided based on previous results from the research group.

5.1.1 Sample preparation technique

All the samples grown on Si(111) were prepared for growth by annealing at 1100°C for 15 minutes, before being cooled to growth temperature. This is done in order to remove the oxide layer which forms on the surface, and is a common technique in epitaxy. The annealing temperature and time was found by analyzing the crystallinity of the surface using RHEED. The RHEED pattern after this preparation process can be seen in the first video still in figure 5.4. The pattern shows that we get clean, nearly flat surfaces in Si(111), indicating that the oxide layer is removed. This allows for high quality, reproducible, stable conditions for starting the growth.

5.1.2 Substrate temperature variation

This section shows the results from the substrate temperature variation series.

Crystal structure analysis

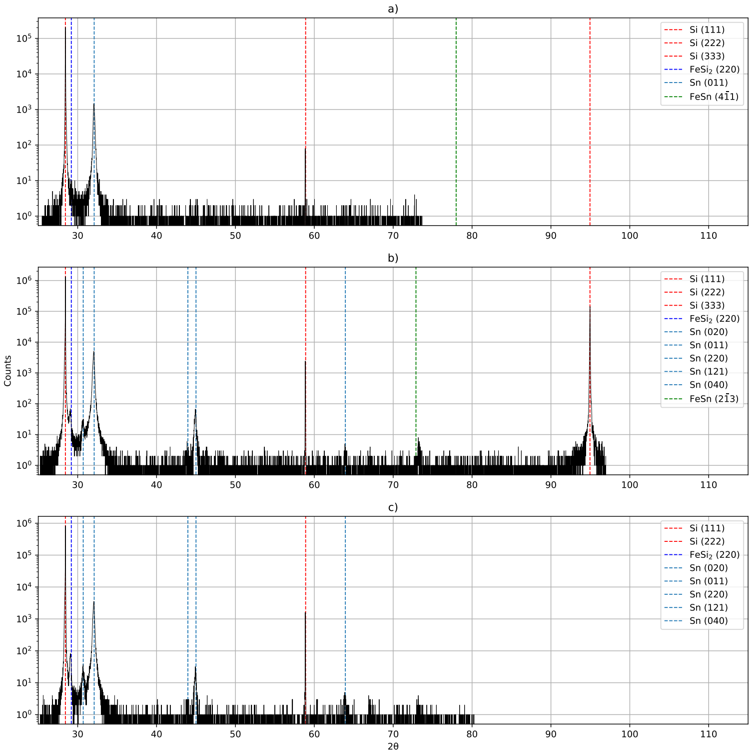

Figure 5.1: X-ray diffraction spectra of samples grown on Si(111) substrates, with (a), (b) and (c) showing the measurements of samples 1, 2 and 3, respectively. Relevant dotted lines are included to show peaks of known phases.

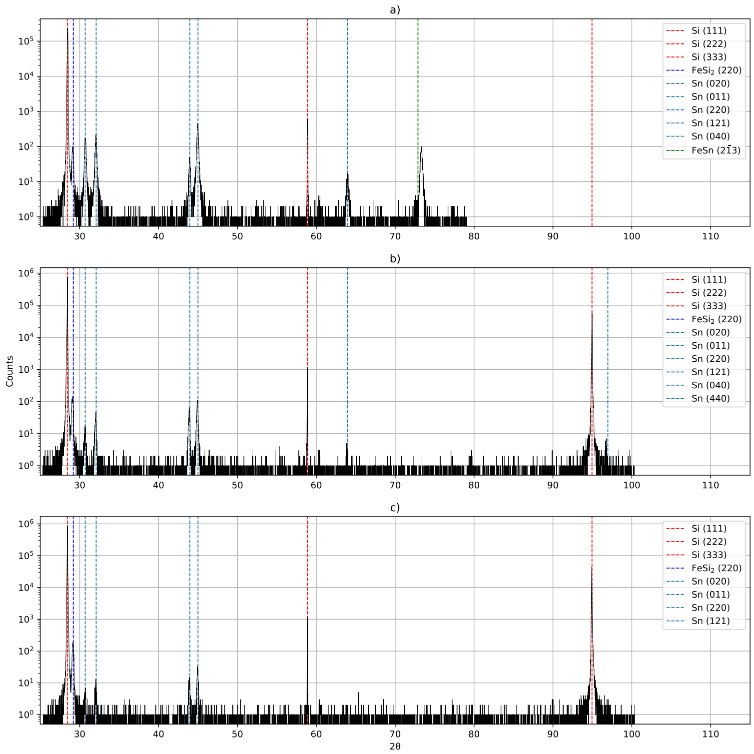

Figure 5.2: X-ray diffraction spectra of samples grown on Si(111) substrates, with with (a), (b) and (c) showing the measurements of samples 4, 5 and 6, respectively. Relevant dotted lines are included to show peaks of known phases.

Figures 5.1 and 5.2 show the XRD spectra for the growth series on Si(111) substrates, with varying substrate temperature. Strong peaks corresponding to phases Si(111), Si(222) and Si(333) are identified for all the samples. They are highlighted by red dotted lines in $2\theta = 28.44°$, $2\theta = 58.90°$ and $2\theta = 94.95°$, respectively. The intensities of these peaks are of similar orders of magnitude for all the samples, with Si(111) and Si(333) around $10^5 - 10^6$ counts, and Si(222) around 10^3 counts. However, the intensity observed for Si(333) in sample 1 is lower (10^2 counts). And for sample 3, Si(333) is not observed, because the data stops after $2\theta = 60°$. The peak intensity of Si(222) being lower than Si(111) and Si(333), independently of the substrate temperature, is consistent with Si(222) being a basis-forbidden reflection [48].

One peak close to Si(111) is observed for all the temperatures, but with varying intensity. It is close to the peak position of $FeSi_2$ for bulk crystals, $2\theta = 29.19°$, and is attributed to that phase. The intensity increases with increasing substrate temperature.

Multiple peaks which are attributed to different planes of the beta phase of tin (β-tin) are observed for all the different temperatures. These peaks are highlighted by in light-blue dotted lines. Sample 4 ($T_{\text{substrate}} = 550°\text{C}$) shows the highest number of these peaks, and with the highest intensities. The presence of β-tin does not increase with increasing substrate temperature.

Additional peaks are observed in the range $2\theta \in (70°, 80°)$, for some of the samples. They are close to known FeSn peaks in $2\theta = 72.89°$ and $2\theta = 77.98°$, and are attributed to that phase. However the peak locations does not match perfectly, as can be seen by comparing with the green dotted lines, so there is greater uncertainty in the indexing of these peaks.

$FeSi_2$ and β-tin phases dominating over any of the phases of the Fe-Sn Kagome system proves that there is an unwanted reaction between iron and the Si(111) substrate, which is not suppressed by changing the substrate temperature.

Surface topology analysis

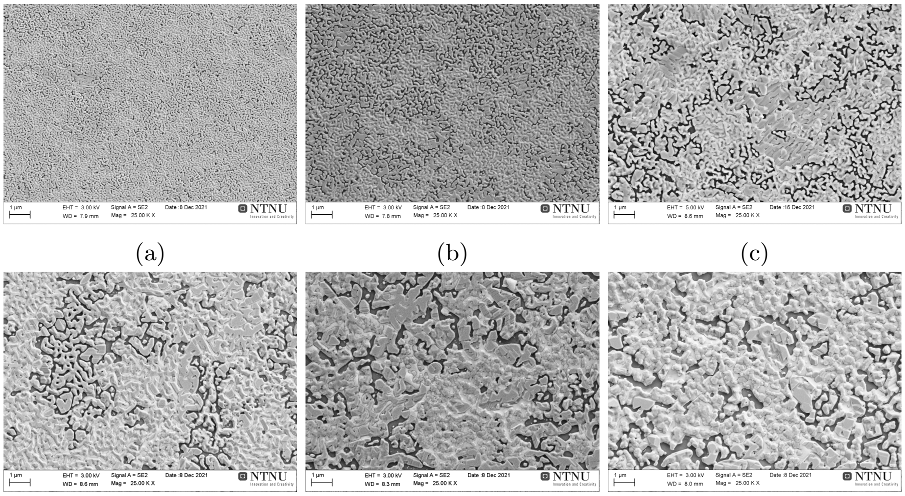

(a) (b) (c)

(d) (e) (f)

Figure 5.3: Images from SEM measurements with magnification 25.00 K X for samples grown on Si(111) substrates, with varying substrate temperatures. With figures (a), (b), (c), (d), (e) and (f) showing measurements of samples 1, 2, 3, 4, 5 and 6, respectively.

SEM measurements of the samples grown on Si(111) substrates with varying substrate temperature (sample 1-6) are included in figures 5.3a, 5.3b, 5.3c, 5.3d, 5.3e, 5.3f. The measurement settings are shown in the figures.

With a substrate temperature $T_{\text{Substrate}} = 400°\text{C}$, figure 5.3a shows a non-uniform surface with no large crystallites. Increasing the temperature reveals patches of differently colored areas on the surface. The darker areas with more structured crystallites attributed to iron silicide, while the lighter areas are attributed to the β-tin phase observed in the crystal structure analysis. The structures increase in size with increasing temperature. The darker structures are separated into crystal islands, with semi-flat surfaces. Figure 5.3e shows the surfaces clearly with lines on top, indicating step-like topology. Comparing 5.3e and 5.3f, it is apparent that 5.3e has a higher iron silicide to β-tin ratio than 5.3f in the specific areas the SEM was measured. This shows the non-uniformity of the different crystal phases on the samples.

This analysis shows that increasing the substrate temperature during growth, improves the quality of the surface topology. Using too low temperatures gives a very non-uniform surface without any large crystallites. With higher temperatures, larger crystal islands appear across the surface. The islands have semi-flat surfaces.

RHEED analysis from sample grown at $\mathbf{T_{Substrate}} = \mathbf{650°}$C

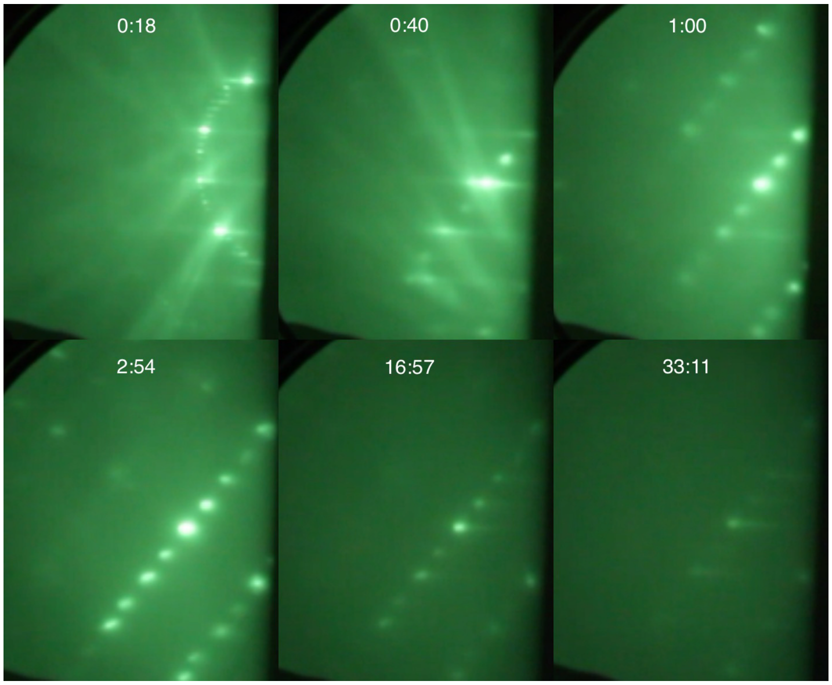

Figure 5.4: Video stills of the RHEED pattern of sample 6, from from 18 seconds, 40 seconds, 1 minute, 2 minutes 54 seconds, 16 minutes 57 seconds and 33 minutes and 11 seconds of growth.

Video stills from the sample grown with substrate temperature $T_{\text{Substrate}} =$ 650°C are presented in figure 5.4. The RHEED pattern after 18 seconds consists of semicircles of many small, very clear dots. Clear Kikuchi lines are also visible. An indication of longer lines through the clearest dots can also be observed. This is attributed to the pure Si(111) substrate, after removing the oxide layer through annealing. After 40 seconds, the RHEED pattern changes from semi-circles to diagonal lines, and the dots appear more diffuse and partial 2D, however still mostly 3D crystal islands. The RHEED pattern after 1 minute and 2 minutes 54 seconds shows the partial 2D pattern disappear, and turn into pure 3D dots. The Kikuchi lines also disappear. The RHEED pattern at times 16:57 and 33:11, respectively show the 2D lines gradually returning.

The transition from 2D growth to 3D, and back to an indication of 2D can be explained by the deposited layer initially being so thin it appears 2D. Then revealing a 3D RHEED pattern when separated crystal islands become larger, and forms a rough surface topology, before the islands merge into semi-flat surfaces, as indicated by the surface topology analysis, and show a combination of 3D and 2D RHEED pattern.

5.1.3 Growth time variation

This section shows the results from the growth time variation series on Si(111). The growth time parameters was explored in order to see how it affected the growth, and especially if it would suppress or otherwise affect the presence of $FeSi_2$ and β-tin in the samples.

Crystal structure analysis

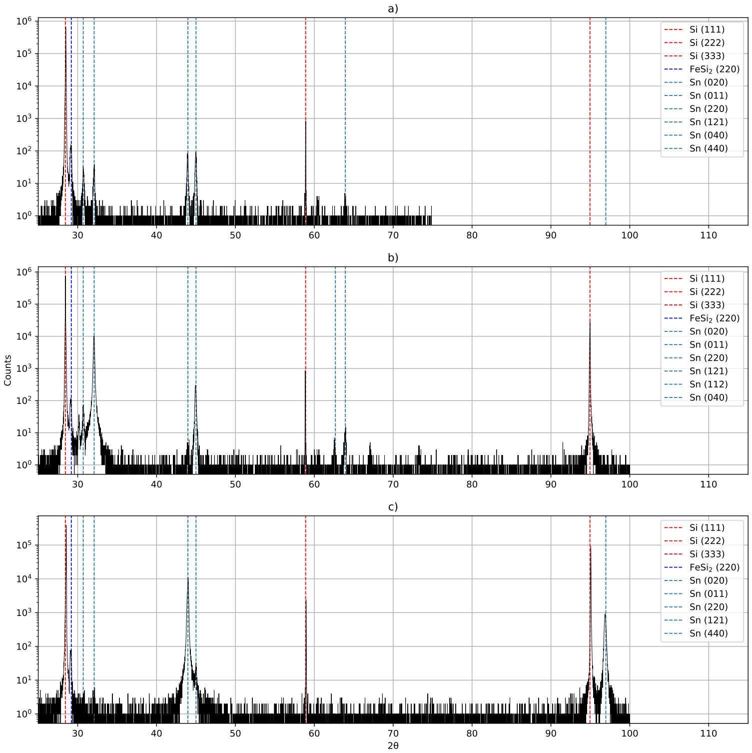

Figure 5.5: X-ray diffraction spectra of samples grown on Si(111) substrates, with with (a), (b) and (c) showing the measurements of samples 7, 8 and 9, respectively. Relevant dotted lines are included to show peaks of known phases.

The XRD spectra of the samples grown on Si(111) substrates with varying growth times are shown in figure 5.5. Strong peaks corresponding to Si(111), Si(222) and Si(333) are identified in all the samples in this series, identical to the previous growth series in section 5.1.2. These peaks are highlighted by red dotted lines in $2\theta = 28.44°$, $2\theta = 58.90°$ and $2\theta = 94.95°$. The peaks have similar intensities as the previous growth series, with Si(111) and Si(333) around $10^5 - 10^6$ counts, and Si(222) around $10^2 - 10^3$ counts, consistent with Si(222) being a basis-forbidden reflection [48].

One peak close to Si(111) is observed, with similar intensities for all three growth times. It is close to the peak position of $FeSi_2$ for bulk crystals, $2\theta = 29.19°$, and is attributed to that phase. The intensity decreases slightly with increasing growth time.

Multiple peaks are identified as different planes of the beta phase of tin (β-tin), as highlighted with light-blue dotted lines. The intensities of the individual peaks varies a lot; sample 8 and 9 has one β-tin peak each with intensity of 10^4 counts, while the rest are of lower intensities.

The crystal structure analysis shows that varying the growth time parameter failed to suppress the reaction between iron and the Si(111) substrate, and allow phases of the Fe-Sn Kagome system to grow.

Surface topology analysis

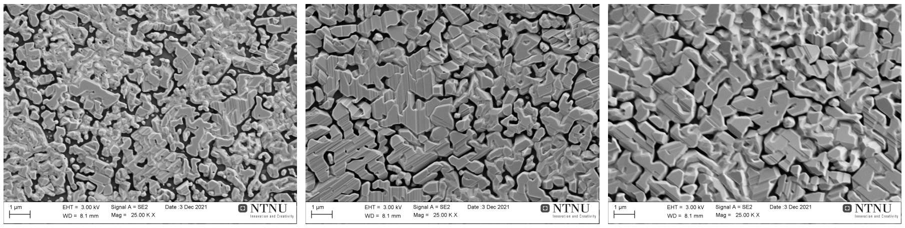

(a) (b) (c)

Figure 5.6: Images from SEM measurements with magnification 25.00 K X for samples grown on Si(111) substrates, with varying growth time. With (a), (b) and (c) showing measurements of samples 7, 8 and 9, respectively.

The SEM measurements from the growth time variation on Si(111) substrates are shown in figures 5.6a, 5.6b and 5.6c. The measurement settings are shown in the figures.

With a growth time of 1 hour, figure 5.6a shows separated crystal islands with semi-flat surfaces, similar to the high temperature results from the previous section. Increasing the growth time to 2 hours, figure 5.6b reveals larger crystal islands. Lines indicating step-like surfaces are clearly visible. The distinction between the two types of crystal structures are made here, identical to the results from the temperature variation. 5.6c shows higher content of of β-tin compared to 5.6b, however, this can be a result of the particular region the SEM image is made from being more saturated in β-tin. During the SEM measurements, other areas on the sample showed the reverse ratio. There is no significant increase in the size of the crystal islands when increasing the growth time from 2 hours to 3 hours.

The SEM analysis shows that varying the growth time affects the surface topology of the crystal growth significantly. Increasing the growth time from 1 to 2 hours makes the semi-flat crystal islands larger and more dominant, however increasing to 3 hours did not show further improvements.

5.1.4 Discussion

The RHEED analysis from sample 6 grown on Si(111) indicates a combination of 3D and 2D growth. However, the surface topology analysis revealed that the apparent 2D growth was crystal islands with flat surfaces. Changing the substrate temperature and growth time proved insufficient to achieve true 2D growth.

The crystal structure analysis showed that none of the samples grown on Si(111) were single-phase crystals. Instead, $FeSi_2$ and β-tin dominated in all the samples, proving there is an unwanted reaction between the Si(111) substrate and the deposited material. This reaction could not be mitigated by changing the substrate temperature and growth time. In conclusion, Si(111) is unsuited for growing high-quality films of the Kagome system Fe-Sn, and instead, other substrates should be explored in the attempt to grow these films.

5.2 Gallium arsenide substrate

This section covers the all the growth series grown on gallium arsenide substrates, with orientation (111). All the relevant parameters for the samples in these series are presented in table 5.2. The material of the substrates was changed in order to avoid the reaction between iron and silicon which dominated in all the samples grown on Si(111).

Table 5.2: Values for the growth parameters for each sample grown on GaAs(111) substrates.

Name	Growth time (minutes)	$T_{\text{Substrate}}$ (°C)	T_{Fe} (°C)	T_{Sn} (°C)
Sample 10	60	350	1400	1100
Sample 11	45	350	1400	1050
Sample 12	60	350	1400	900
Sample 13	60	325	1400	900
Sample 14	180	325	1400	900
Sample 15	180	325	1400	950
Sample 16	180	325	1350	950
Sample 17	120	325	1300	1000
Sample 18	300	325	1350	950
Sample 19	300	300	1350	950

Ding et al. has developed a computational framework [49] based on minimal coincident interface area, for finding optimal substrates for epitaxial growth. The results of these calculations for the hexagonal plane (001) of Fe_3Sn_2 are presented in [50]. GaAs(111) is on the list as a suitable substrate, with minimal coincident interface area of 172.3 [50].

Another way of predicting if a substrate is suited for growing a specific crystal, is to calculate the lattice matching. A large lattice mismatch can lead to ATG instabilities (see section 3.4), which can reduce the film quality and hinder the growth.

Lattice matching comparison of gallium arsenide and silicon

The lattice constants of Fe_3Sn_2, with respect to the tripled hexagonal unit cell, are $a = b = 5.3145$Å, $c = 19.7025$Å [17]. For cubic silicon, as in Si(111) substrates, the lattice constants are $a = b = c = 3.867$Å [51]. And the lattice constants for cubic gallium arsenide are $a = b = c = 4.066$Å [52]. The lattice mismatch with the substrate can be calculated with the equation [53]

$$\Delta = \frac{a_{sub} - a_{epi}}{a_{sub}}. \tag{5.1}$$

Calculating the strain caused by the lattice mismatch between the different substrates and Fe_3Sn_2, we get

$$\Delta_{\mathrm{Si}\to\mathrm{Fe_3Sn_2}} = \frac{3.867\text{Å} - 5.3145\text{Å}}{3.867\text{Å}} \approx -37.43\%$$

$$\Delta_{\mathrm{GaAs}\to\mathrm{Fe_3Sn_2}} = \frac{4.066\text{Å} - 5.3145\text{Å}}{4.066\text{Å}} \approx -30.71\%$$

where $\Delta_{\mathrm{Si}\to\mathrm{Fe_3Sn_2}}$ is the lattice mismatch between the silicon substrate and Fe_3Sn_2, given as a percentage, while $\Delta_{\mathrm{GaAs}\to\mathrm{Fe_3Sn_2}}$ is the same property, calculated for the GaAs substrate.

The lattice mismatch of the GaAs(111) substrate is significantly lower than that of the Si(111) substrate. However, the mismatch is still very large, as typical values are in the range of 2% – 5% [34].

5.2.1 Sample preparation techniques

The direct high-temperature pre-annealing technique used for the preparation of the Si(111) wafers would not work for GaAs substrates. This is because the vapor pressure of arsenic is so high that it causes thermal instability on the substrate for temperatures above 370°C [54], which is below the temperatures needed for heating off the oxide layer. It was found through RHEED pattern analysis that the GaAs(111) wafers turned crystalline after heating at 700°C for around 30s, and remained crystalline throughout the cooldown process to growth temperature, as long as it was under a tin flux beam of sufficient intensity.

The thermal instability of the GaAs(111) substrate is also why the substrate temperature for this growth series is limited to lower temperatures than the Si(111) series.

5.2.2 Tin flux calibration

This section shows the results from the tin flux calibration series on GaAs(111). The Sn evaporation cell was changed between developing the sample preparation technique for the GaAs(111) samples, and the next growth series, meaning the tin flux required for stabilizing the GaAs(111) surface had to be found. This was achieved by systematically reducing the tin flux and recording the RHEED patterns during the cooldown, for different samples.

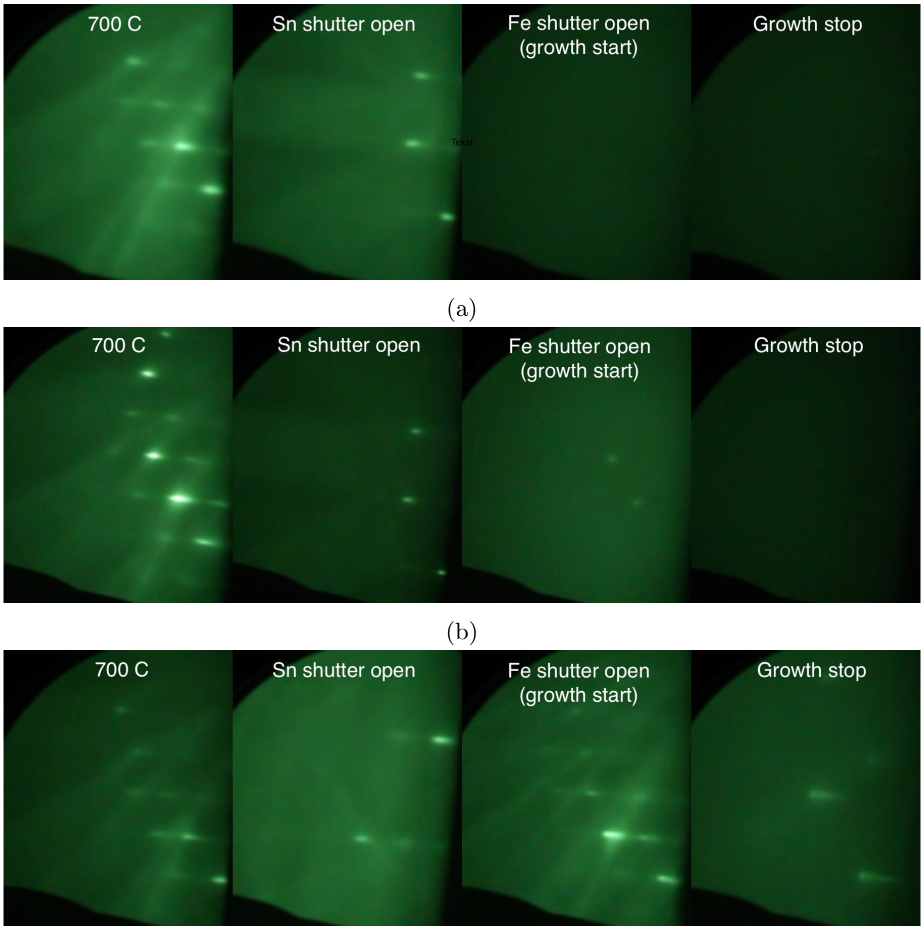

(a)

(b)

(c)

Figure 5.7: Video stills of the RHEED pattern of samples 10, 11 and 12, taken at different stages of the substrate preparation. With (a), (b) and (c) showing the RHEED patterns of samples 10, 11 and 12, respectively.

Figures 5.7a, 5.7b and 5.7c shows the RHEED pattern from different points in the growth start technique, of samples with varying tin flux. Right after reaching $T_{\text{substrate}} = 700$°C, the RHEED pattern of all three samples develop into streaks. The streaks are partly modulated streaks (see section 4.1). Kikuchi lines are also visible.

The tin shutter is opened around 30 seconds after reaching 700°C. Right after opening the tin shutter, the pattern is weaker in intensity. Modulated streaks are still visible in the RHEED pattern for sample 12, while only very weak dots for sample 11. Sample 10 is a combination of modulated streaks and dots. The iron shutter was opened when the substrate temperature had cooled to growth temperature, after around 8 minutes. The RHEED pattern of sample 10 shows no dots, and is completely amorphous. It stays amorphous until growth stop. Sample 11 shows very weak dots initially after opening the iron shutter, however, then it turned amorphous. The modulated streaks in sample 12 are still visible when the iron shutter is opened, and developed small streaks that lasted until growth stop.

In conclusion, sample 12 with $T_{\text{Sn}} = 900$°C stabilized the GaAs(111) substrate successfully during the cooldown, resulting in lasting 2D growth.

5.2.3 Substrate temperature optimization

This section shows the results from the substrate temperature optimization on GaAs(111). Lowering the substrate temperature was tried to see if the growth start conditions could be improved further.

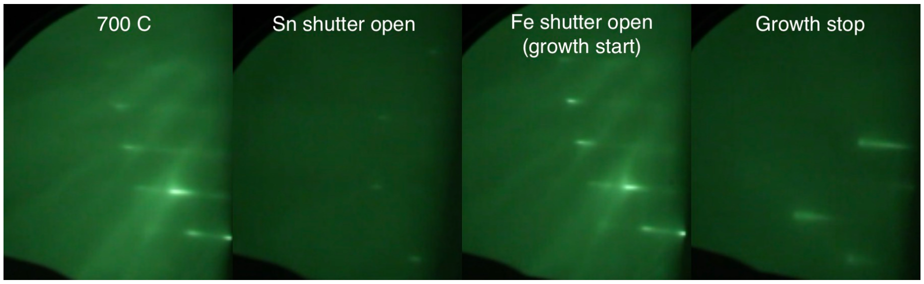

Figure 5.8: Video stills of the RHEED pattern of sample 13, taken at different stages of the substrate preparation.

Figure 5.8 shows partly modulated streaks in the RHEED patterns from substrate temperature $T_{\text{substrate}} = 700$°C until the opening of the iron shutter, similar to sample 12 in figure 5.7c. After starting growth, the RHEED pattern developed into small streaks. Compared to sample 12, the streaks from the diffraction pattern in sample 13 were larger and more numerous.

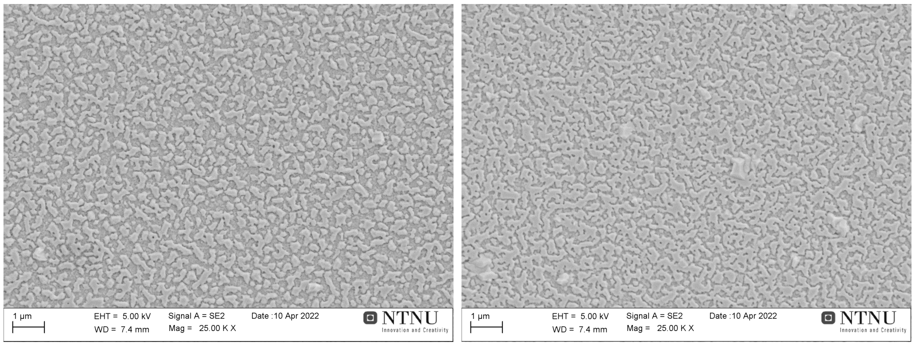

(a) (b)

Figure 5.9: Images from SEM measurements with magnification 25.00 K X for samples grown on GaAs(111) substrates, with parameters given in table 5.2. With (a) and (b) showing the measurements of samples 12 and 13, respectively.

SEM measurements from sample 12 and sample 13 are shown if figures 5.9a and 5.9b, respectively. Both samples consist of separated crystal islands, as the figures show. The sizes of the crystal islands are of the order of magnitude of around $0.1 - 1\mu\text{m}$. However, comparing the two surfaces, it is apparent that the sample with lower substrate temperature has larger crystal islands, that have merged together more.

The growth start procedure is optimized by first finding a tin flux sufficient to stabilize the GaAs(111) surface during the cooldown from the annealing temperature of $T_{\text{substrate}} = 700°\text{C}$. Further improvements were found when decreasing the substrate temperature by 25°C. The success of the substrate surface stabilization under the tin flux, was determined based on how well the RHEED pattern remained crystalline. The distinction between the amorphous RHEED patterns of samples 10 and 11, shown in figures 5.7a and 5.7b, and the streaky RHEED pattern of sample 5.7c is clear.

However, there is more uncertainty when comparing the quality of the growth of sample 12 and sample 13. Although sample 13 exhibits more numerous and larger streaks, the SEM measurements show similar surface structures with crystal islands for both samples in figures 5.9a and 5.9b, even though the crystal islands in sample 13 are larger and with a larger flat surface. The difference might be a result of more material being deposited, as less is re-evaporated when the substrate temperature is lower, instead of real differences in the film quality.

5.2.4 Increasing tin to iron flux ratio

With established parameters for optimal growth start procedures, the next step is to attempt to grow Fe_3Sn_2. This section shows the results from this series on GaAs(111).

The first samples which were attempted showed no peaks in the diffraction patterns from the XRD measurements, except for those attributed to the substrate. This indicates that the samples grown were too thin to study the crystal structures. In order to allow for meaningful crystal structure analysis, the growth time was increased significantly to increase the sample thickness.

Increasing the tin to iron flux ratio for the following series was decided based on the results from the elemental analysis of samples 14 and 15, which is presented below.

Elemental analysis

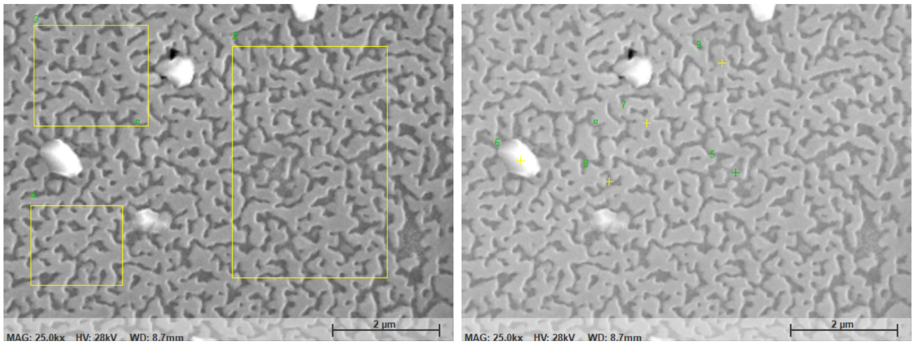

Figure 5.10: SEM measurements with magnification 25.00 K X for sample 14, showing the spectra of the EDS measurements presented in table 5.3.

Table 5.3: Measured values of the atomic contents for the different spectra from the EDS measurements of sample 14.

Spectrum	Ga [%]	As [%]	Fe [%]	Sn [%]
2	45.12	44.22	10.55	0.04
3	45.79	42.78	11.29	0.12
4	45.41	43.26	11.24	0.08
6	40.53	39.16	15.44	4.85
7	47.09	45.16	7.09	0.06
8	44.07	41.65	13.29	0.19
9	46.44	44.64	8.40	0.03

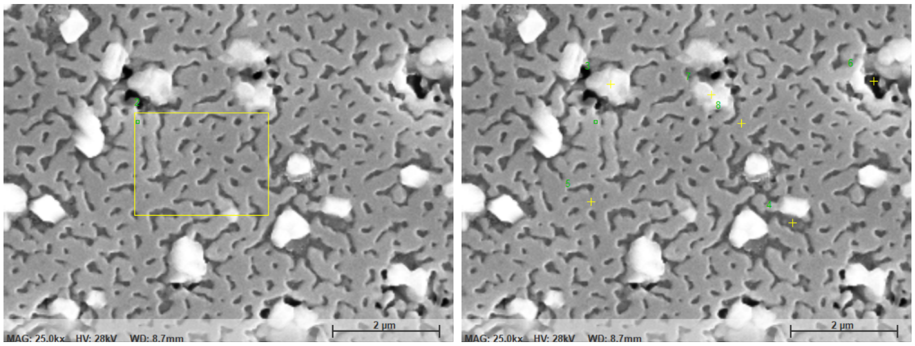

Figure 5.11: SEM measurements with magnification 25.00 K X for sample 15, showing the spectra of the EDS measurements presented in table 5.4.

Table 5.4: Measured values of the atomic contents for the different spectra from the EDS measurements of sample 15.

Spectrum	Ga [%]	As [%]	Fe [%]	Sn [%]
2	45.63	42.87	11.15	0.35
3	41.82	43.35	12.16	2.67
4	45.16	42.61	11.79	0.44
5	45.00	42.64	12.13	0.23
6	42.91	42.56	14.00	0.53
7	45.23	42.58	11.72	0.47
8	45.49	41.48	12.62	0.41

Energy-dispersive X-ray spectroscopy measurements of sample 14 are shown in figure 5.10 and table 5.3, while figure 5.11 and table 5.4 show the results from sample 15. Multiple measurements were conducted on each sample, and the atomic contents of Ga, As, Fe and Sn from all the spectra can be seen in the tables. The SEM figures show the areas of the crystal surface which were scanned, for all the different spectra.

The average iron contents across all the spectra from sample 14 is 11.04%, while the measurements from sample 15 shows an average iron content of 12.22%. The average tin contents of sample 14 is 0.77%, and 0.73% for sample 15, according the the measurements presented in tables 5.3 and 5.4.

The measurements show that iron is successfully deposited on the crystals for both sample 14 and 15. However, almost no tin has been deposited on either sample, even after increasing the tin cell temperature from $T_{\mathrm{Sn}} = 900^{\circ}\mathrm{C}$ (sample 14) to $T_{\mathrm{Sn}} = 950^{\circ}\mathrm{C}$ (sample 15). In order to achieve the stoichiometric composition of $\mathrm{Fe_3Sn_2}$, 3:2 (see section 3.3), the tin to iron flux ratio needs to be increased. T_{Sn} and T_{Fn} are adjusted accordingly for the following samples, and the results are presented in the sections below.

Crystal structure analysis

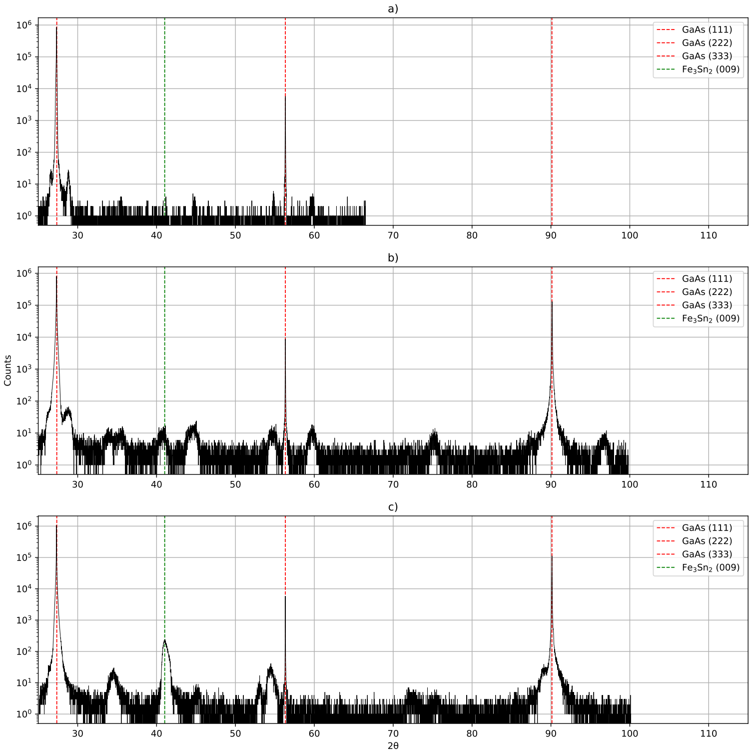

Figure 5.12: X-ray diffraction spectra of samples grown on GaAs(111) substrates, with growth parameters given in table 5.2. (a), (b) and (c) shows the measurements of samples 14, 15 and 16, respectively.

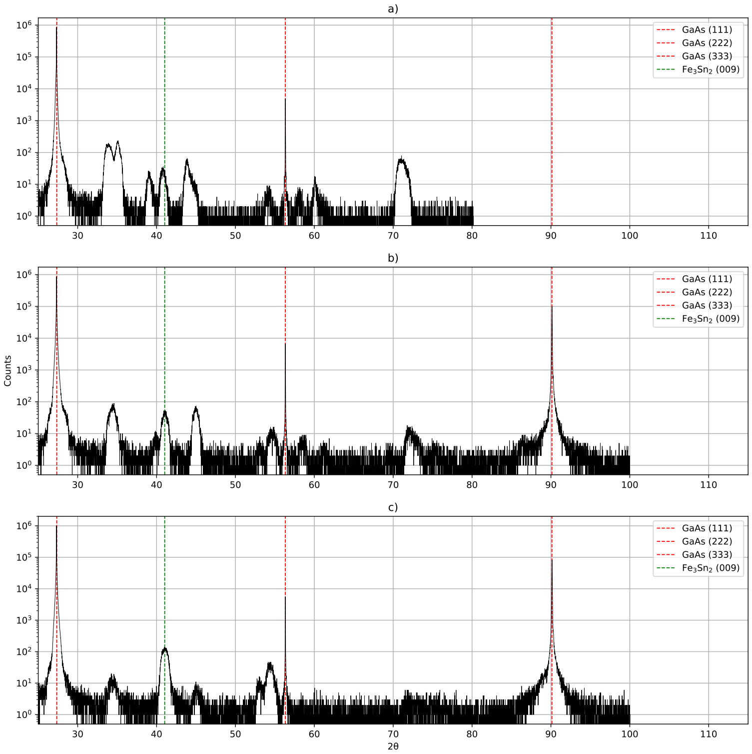

Figure 5.13: X-ray diffraction spectra of samples grown on GaAs(111) substrates, with growth parameters given in table 5.2. (a), (b) and (c) shows the measurements of samples 17, 18 and 19, respectively.

Figures 5.12 and 5.13 show the XRD spectra for the growth series grown on GaAs(111) substrates, with increasing tin to iron flux ratio. Strong peaks corresponding to phases of GaAs(111), GaAs(222) and GaAs(333) are identified for all the samples, corresponding to the substrate. The GaAs(111) peak observed is located in $2\theta = 27.35°$, GaAs(222) in $2\theta = 56.33°$, and GaAs(333) in $2\theta = 90.13°$. The intensities of these peaks are of similar orders of magnitude for all the samples, irrespective of the relative flux ratios of Fe and Sn applied during growth. The GaAs(222) peak appears very narrow, compared with the peaks of GaAs(111) and GaAs(333), indicating that it is a basis-forbidden reflection, similar to Si(222) from the previous growth series (see section 5.1, with figures 5.1, 5.2 and 5.5).

Peaks corresponding to Fe_3Sn_2(009) are observed in samples 15, 16, 17, 18 and 19, and are highlighted in the figures. Samples 14, 15, 16 and 17 shows the $\mathrm{Fe_3Sn_2}$(009) peak increasing in intensity, with increasing tin to iron flux ratio, up to sample 16, and decreasing when increasing the ratio even more in sample 17. Sample 16, with $T_{\mathrm{Fe}} = 1350$°C and $T_{\mathrm{Sn}} = 950$°C, appears to yield the best results, according to the XRD data.

Sample 18 shows the effect of increasing the growth time, with the other parameters being identical to sample 16. The peak corresponding to $\mathrm{Fe_3Sn_2}$(009) in the diffraction pattern of sample 18 has slightly less intensity than in sample 16. Additionally, other unidentified peaks are also of higher intensity, comparatively. This indicates that increasing the growth time from 3 hours to 5 hours, with these parameters, does not increase the presence of $\mathrm{Fe_3Sn_2}$. Furthermore, sample 19 decreases the substrate temperature from sample 18 by 25°C. This shows very similar diffraction pattern to sample 16, both in terms of the intensity of $\mathrm{Fe_3Sn_2}$(009), as well as the presence of other phases with lower intensities.

The other peaks in the diffraction patterns of samples 14, 15, 16, 17, 18 and 19 are unidentified. The combination of GaAs, Fe and Sn has too many possible phases with peaks in similar positions, to uniquely index the peaks observed, without additional measurements.

Additionally, there are uncertainties in XRD measurements, which makes it difficult to draw definitive conclusions on the differences between, for instance, samples 16, 18 and 19. The most notable difference between these XRD patterns are the relative peak intensities. However, this could be artefacts instead of real differences.

For zincblende crystals, like the Si and GaAs substrates, (111) is the hexagonal plane. While for structures like $\mathrm{Fe_3Sn_2}$, the hexagonal plane is in the (001) direction. The results show that the hexagonal orientation of $\mathrm{Fe_3Sn_2}$ was successfully deposited on the hexagonal oriented GaAs(111) substrates. This means that the thin films are deposited along the c-direction (see section 2.3.1), which is the orientation required for 2D skyrmions in this system. However, in order to achieve single-crystalline $\mathrm{Fe_3Sn_2}$, the unidentified phases needs to be suppressed. Additionally, an atomically flat crystal surface morphology is needed to measure the magnetic properties of the film with MFM.

Surface topology analysis

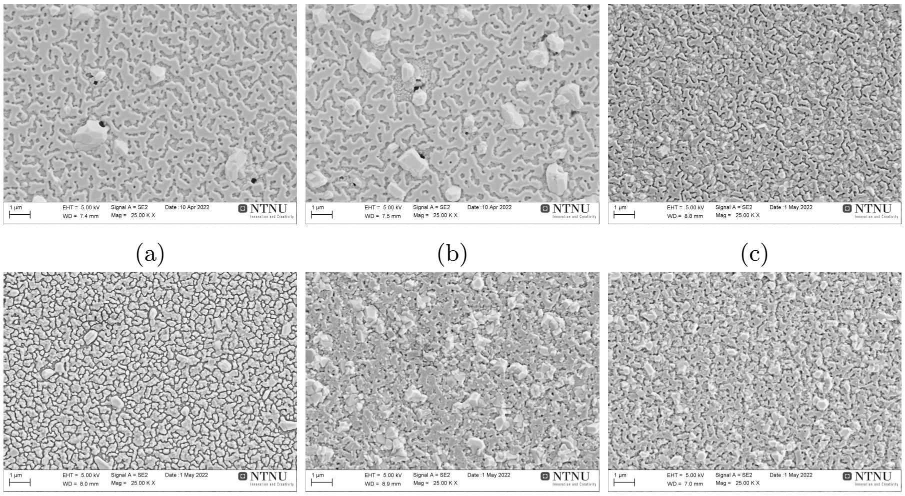

(a) (b) (c)

(d) (e) (f)

Figure 5.14: Images from SEM measurements with magnification 25.00 K X for samples grown on GaAs(111) substrates, with parameters given in table 5.2. With (a), (b), (c), (d), (e) and (f) showing measurements of samples 14, 15, 16, 17, 18 and 19, respectively.

Figures 5.14a, 5.14b, 5.14c and 5.14d show the SEM measurements of the samples grown on GaAs(111) substrates with increasing tin to iron flux ratio. The surface of sample 14 consists of a large connected smooth surface, with lots of holes, revealing a less smooth textured lower layer, which is assumed to be amorphous. Larger crystal islands with sizes on the order of magnitude of 1µm appear randomly across the surface. Approximately 9 large crystal bumps are visible in the area imaged in figure 5.14a.

Increasing the tin flux (figure 5.14b), affects the surface topology little. The holes in the large flat structure appear smaller and less frequently. Additionally, the amount of crystal islands have more than doubled, with approximately 24 being visible in the imaged area in the figure.

5.14c shows the effects of decreasing the iron flux. The surface is more rough, with no large continuous structure with a flat surface. The surface consists of many smaller crystallites, with the longest continuous surface being around 2µm. There are no large crystal islands in the imaged area, as was observed in samples 14 and 15. The amorphous background layer is still present, however, it is more mixed with small crystallites.

Sample 17 shows the surface of the sample grown with the highest tin to iron flux ratio. It consists of clusters of very small crystals in different orientations. Some larger crystal islands appear on the surface, similar to those observed in samples 14 and 15. The background layer is darker and more less textured.

Figure 5.14e shows the surface topology after longer growth time, and 5.14f shows the effect of reducing the substrate temperature further. The iron and tin fluxes of these are identical to sample 16, which is imaged in figure 5.14c. The surface of sample 18 is a combination of large semi-flat structures, and 3D crystals of varying sizes. The semi-flat surfaces has lines indicating a step-like topology. And, comparatively, sample 19 shows a similar surface, however, with less prominent semi-flat structures, and more smaller 3D crystals.

In conclusion, the surface topology of the samples grown on GaAs(111) substrates was not atomically flat. This means that the $Fe_3Sn_2(009)$ that was observed did not grow 2D, layer-by-layer. To achieve this, new growth parameter regimes must be explored, in further work. However, it might be beneficial to first optimize for single-crystalline films of $Fe_3Sn_2(009)$ by suppressing the unidentified peaks discussed in the crystal structure analysis, after correctly indexing them.

Chapter 6

Conclusion and outlook

Si(111) was shown to be an unsuitable substrate for growing thin films of Fe_3Sn_2. The iron atoms reacted with the silicon substrate and formed $FeSi_2$, in addition to phases of β-tin. These reactions dominated over other phases, which suppressed Fe_3Sn_2. Varying the substrate temperature and growth time did not reduce the unwanted reactions.

Strong peaks of Fe_3Sn_2 were found using GaAs(111), with certain parameters. Initially, the flux ratio of Sn was too low, however, this was adjusted after conducting EDS measurements, and comparing with the stoichiometric composition of Fe_3Sn_2. The best results were found with $T_{\text{Fe}} = 1350°\text{C}$, $T_{\text{Sn}} = 950°\text{C}$, $T_{\text{substrate}} = 950°\text{C}$ and a growth time of 180 minutes (sample 16 in table 5.2).

The Fe_3Sn_2 phases observed in the GaAs(111), were $Fe_3Sn_2(009)$, which is in the (001)-direction. This means that the thin films grew along the stacking of the Kagome layers in the crystal structure (c-direction in section 2.3.1). This is the correct orientation for 2D out-of-plane skyrmions. However, other unidentified phases were also present in all the samples, according to the XRD measurements in the crystal structure analysis. These phases remained unidentified because of the large number of possible peaks in similar positions, from all the combinations of GaAs, Fe and Sn, in addition to limited analysis software. In order to achieve single-crystalline Fe_3Sn_2, the unidentified phases needs to be suppressed.

Furthermore, the films showed a varying degree of surface roughness, but no set of parameters achieved an atomically flat 2D surface. This would be required to measure the magnetic properties of the surface with MFM, to be able to detect the magnetic skyrmions in the film.

For further work, it would also be useful to grow thin films of $Fe_3Sn_2(111)$, in order to study the quantum properties of this structure to explore the possibility for future technological applications. The computational framework for matching film to a substrate, developed by Ding et al. [49], can be used to find a substrate more suitable for growing $Fe_3Sn_2(111)$. And according to the data presented in [50], the optimal substrate to grow this phase is $BaTiO_3(100)$. However, this material is orders of magnitude more expensive than Si(111) and

GaAs(111), and is likely of lesser crystal and surface quality, which would complicate the synthesis of this phase of Fe_3Sn_2(111).

Bibliography

[1] Stuart S. P. Parkin, Masamitsu Hayashi, and Luc Thomas. Magnetic domain-wall racetrack memory. *Science*, 320(5873):190–194, 2008.

[2] Gordon E. Moore. Cramming more components onto integrated circuits. *Electronics*, 38(8):114–117, 1965.

[3] Robert H. Dennard, Fritz H. Gaensslen, Hwa nien Yu, V. Leo Rideout, Ernest Bassous, Andre, and R. Leblanc. Design of ion-implanted mosfets with very small physical dimensions. *IEEE J. Solid-State Circuits*, page 256, 1974.

[4] Adrian McMenamin. The end of dennard scaling. Accessed: 14-12-2021.

[5] Suhas Kumar. Fundamental limits to moore's law, 2015.

[6] Jongyeon Kim, Ayan Paul, Paul A. Crowell, Steven J. Koester, Sachin S. Sapatnekar, Jian-Ping Wang, and Chris H. Kim. Spin-based computing: Device concepts, current status, and a case study on a high-performance microprocessor. *Proceedings of the IEEE*, 103(1):106–130, 2015.

[7] A. Bogdanov and D. Yablonskiui. Thermodynamically stable "vortices" in magnetically ordered crystals. the mixed state of magnets. *Sov. Phys. JETP*, 68:101, 01 1989.

[8] T. H. R. Skyrme. A unified field theory of mesons and baryons. *Nuclear Physics*, 31:556–569, 1962.

[9] S. Mühlbauer, B. Binz, F. Jonietz, C. Pfleiderer, A. Rosch, A. Neubauer, R. Georgii, and P. Böni. Skyrmion lattice in a chiral magnet. *Science*, 323(5916):915–919, 2009.

[10] Zhipeng Hou, Weijun Ren, Bei Ding, Guizhou Xu, Yue Wang, Bing Yang, Qiang Zhang, Ying Zhang, Enke Liu, Feng Xu, Wenhong Wang, Guangheng Wu, Xi xiang Zhang, Baogen Shen, and Zhidong Zhang. Observation of various and spontaneous magnetic skyrmionic bubbles at room-temperature in a frustrated kagome magnet with uniaxial magnetic anisotropy. *Advanced Materials*, 29(29):1701144, August 2017.

[11] Hisashi Inoue, Minyong Han, Linda Ye, Takehito Suzuki, and Joseph. G. Checkelsky. Molecular beam epitaxy growth of antiferromagnetic kagome metal fesn. *Applied Physics Letters 115, 072403 (2019).*

[12] W. Patrick McCray. MBE deserves a place in the history books. *Nature nanotechnology*, 2 5:259–61, 2007.

[13] David K. Cheng. *Field And Wave Electromagnetics 2nd Edition.* Addion-Wesley Publishing Company, 1983.

[14] Alex Hubert and Rudolf Schafer. *Magnetic Domains: The Analysis of Magnetic Microstructures.* Springer, 1998.

[15] Wolfgang Nolting and Anupuru Ramakanth. *Quantum Theory of Magnetism.* Springer, 2009.

[16] Börge Göbel, Ingrid Mertig, and Oleg A. Tretiakov. Beyond skyrmions: Review and perspectives of alternative magnetic quasiparticles. *Physics Reports 895, 1*, 2020.

[17] L. A. Fenner, A. A. Dee, and A. S. Wills. Non-collinearity and spin frustration in the itinerant kagome ferromagnet Fe_3Sn_2. *Journal of Physics: Condensed Matter*, 21(45):452202, oct 2009.

[18] Manuel Pereiro, Dmitry Yudin, Jonathan Chico, Corina Etz, Olle Eriksson, and Anders Bergman. Topological excitations in a kagome magnet. *Nat. Commun. 5, 4815 (2014).*

[19] T. Kida, L. A. Fenner, A. A. Dee, I. Terasaki, M. Hagiwara, and A. S. Wills. The giant anomalous hall effect in the ferromagnet Fe_3Sn_2. *Journal of Physics: Condensed Matter*, 23(11):112205, 2011.

[20] Linda Ye, Mingu Kang, Junwei Liu, Felix von Cube, Christina R. Wicker, Takehito Suzuki, Chris Jozwiak, Aaron Bostwick, Eli Rotenberg, David C. Bell, Liang Fu, Riccardo Comin, and Joseph G. Checkelsky. Massive Dirac fermions in a ferromagnetic kagome metal. *Nature 555, 638-642 (2018).*

[21] Linda Ye, Mun K. Chan, Ross D. McDonald, David Graf, Mingu Kang, Junwei Liu, Takehito Suzuki, Riccardo Comin, Liang Fu, and Joseph G. Checkelsky. de Haas-van Alphen effect of correlated Dirac states in kagome metal Fe_3Sn_2. *Nature Communications 10, 4870 (2019)*, 2018.

[22] P.A. Redhead, J.P. Hobson, and E.V. Kornelsen. Ultrahigh vacuum. volume 17 of *Advances in Electronics and Electron Physics*, pages 323–431. Academic Press, 1963.

[23] Normand M. Laurendeau. *Statistical Thermodynamics: Fundamentals and Applications.* Cambridge University Press, 2006.

[24] Secondo Franchi. *Molecular beam epitaxy.* Elsevier, Oxford, 2013.

[25] Ltd. Kashiyama Industries. Neodry e series, 2 2022.

[26] Gary S. Ash. Handbook of vacuum science and technology. *Academic Press*, pages 149–182, 1998.

[27] Austin Chambers. *Modern Vacuum Physics*. Masters series in physics and astronomy. CRC Press, Boca Raton, FL, August 2004.

[28] MBE-Komponenten GmbH Dr. Eberl. Selection guide: Element, 2022.

[29] MBE-Komponenten GmbH Dr. Eberl. Selection guide: Iron, 2022.

[30] MBE-Komponenten GmbH Dr. Eberl. Selection guide: Tin, 2022.

[31] Shuyu Cheng, Igor Lyalin, Alexander J. Bishop, and Roland K. Kawakami. Epitaxial growth and domain structure imaging of kagome magnet Fe_3Sn_2, 2021.

[32] F. Briones and A. Ruiz. Atomic layer molecular beam epitaxy. *Journal of Crystal Growth*, 111(1):194–199, 1991.

[33] Tatau Nishinaga. *Handbook of Crystal Growth (Second Edition)*. North-Holland, Boston, 2015.

[34] A. Danescu. The Asaro–Tiller–Grinfeld instability revisited. *International Journal of Solids and Structures*, 38(26):4671–4684, 2001.

[35] John Norton and Tom Foxon. *Molecular beam epitaxy*. Oxford University Press, 2015.

[36] Shuji Hasegawa. *Reflection high-energy electron diffraction*. John Wiley & Sons, Inc., Hoboken, NJ, USA, October 2012.

[37] A. Y. Cho. Epitaxy by periodic annealing. *Surface Science*, 17(2):494–503, 1969.

[38] A. Y. Cho. Epitaxial growth of gallium phosphide on cleaved and polished (111) calcium fluoride. *Journal of Applied Physics*, 41(2):782–786, 1970.

[39] A. Y. Cho. Morphology of epitaxial growth of gaas by a molecular beam method: The observation of surface structures. *J. Appl. Phys.*, 41(7):2780–2786, jun 1970.

[40] A. Y. Cho and I. Hayashi. Surface structures and photoluminescence of molecular beam epitaxial films of gaas. *Solid-State Electronics*, 14(2):125–132, 1971.

[41] A. Y. Cho. Gaas epitaxy by a molecular beam method: Observations of surface structure on the (001) face. *Journal of Applied Physics*, 42:2074–2081, 1971.

[42] A. Y. Cho. Film deposition by molecular-beam techniques. *Journal of Vacuum Science and Technology*, 8(5):S31–S38, 1971.

[43] A. Y. Cho and J. R. Arthur. Molecular beam epitaxy. *Progress in solid state chemistry*, 10:157–191, 1975.

[44] J.J. Harris, B. A. Joyce, and P.J. Dobson. Oscillations in the surface structure of Sn-doped GaAs during growth by MBE. *Surface Science*, 103(1):L90–L96, 1981.

[45] T. Kawamura and P.A. Maksym. Origin of RHEED intensity oscillation during homoepitaxial growth on Si(001). *Surface Science*, 630:125–135, 2014.

[46] George F. Harrington and José Santiso. Back-to-basics tutorial: X-ray diffraction of thin films. *J. Electroceram.*, October 2021.

[47] Henry G. J. Moseley. XCIII. The high-frequency spectra of the elements. *The London, Edinburgh, and Dublin Philosophical Magazine and Journal of Science*, 26(156):1024–1034, 1913.

[48] Peter Zaumseil. High-resolution characterization of the forbidden Si 200 and Si 222 reflections. *Journal of Applied Crystallography*, 48(2):528–532, Apr 2015.

[49] Hong Ding, Shyam S. Dwaraknath, Lauren Garten, Paul Ndione, David Ginley, and Kristin A. Persson. Computational approach for epitaxial polymorph stabilization through substrate selection. *ACS Applied Materials & Interfaces*, 8(20):13086–13093, 2016. PMID: 27145398.

[50] Kristin Persson. Materials Data on Fe_3Sn_2 by Materials Project, 2016.

[51] Kristin Persson. Materials Data on Si by Materials Project, 2014.

[52] Kristin Persson. Materials Data on GaAs by Materials Project, 2014.

[53] A. Trampert, O. Brandt, and K.H. Ploog. *Chapter 7 Crystal Structure of Group III Nitrides*, volume 50. Elsevier, 1997.

[54] Leonid Miroshnik, Brian D. Rummel, Andrew B. Li, Ganesh Balakrishnan, Talid Sinno, and Sang M. Han. Maintaining atomically smooth GaAs surfaces after high-temperature processing for precise interdiffusion analysis and materials engineering. *Journal of Vacuum Science & Technology B*, 39(6):062212, 2021.

List of Figures

ß

List of Tables

NTNU

Norwegian University of
Science and Technology